1990

Development and evaluation of an adaptive volume puff model

Z. (Zafer) Boybeyi
San Jose State University

Order Number 1340497

Development and evaluation of an adaptive volume puff model

Boybeyi, Zafer, M.S.

San Jose State University, 1990

U·M·I

300 N. Zeeb Rd.
Ann Arbor, MI 48106

DEVELOPMENT AND EVALUATION OF AN ADAPTIVE VOLUME PUFF MODEL

A Thesis

Presented to

the Faculty of the Department of Meteorology

San Jose State University

In Partial Fulfillment

of the Requirements for the Degree

Master of Science

By

Zafer Boybeyi

May 1990

APPROVED FOR THE DEPARTMENT OF METEOROLOGY

R. Bornstein

APPROVED FOR THE UNIVERSITY

Serena H. Stanford

ABSTRACT

The Adaptive Volume Plume Model has been modified to locate systematically (at every time step) pollutants previously emitted into a complex meteorological field. A movable fine mesh computational grid is then established around the material in several steps that involve determining the absolute concentration field using an estimated "relative" concentration field. The model was tested for an instantaneous (10 min) release producing a single puff, so that its behavior could be easily evaluated under various complex meteorological conditions. Model results generally reproduce steady-state analytical Gaussian concentrations. Complicated puff shapes caused by wind speed and directional shear, subsidence, and fumigation conditions are generally well represented by the model. Two areas in which the model formulation should be improved were identified, i.e., the upper and lower bounds of the simulated pollutant mass should be extended, and diffusion coefficients should depend on travel time, rather than travel distance to provide a more realistic simulation of very low wind speed conditions.

ACKNOWLEDGEMENTS

I wish to thank Bob Bornstein of San Jose State University for suggesting the work and for his assistance throughout the project. I also would like to thank Francis Ludwig of SRI, International for his many helpful suggestions. Finally, I would like to thank Andrea Debbs for her expert word processing of the manuscript.

TABLE OF CONTENTS

1. INTRODUCTION

Air quality dispersion models are either Eulerian or Lagrangian in their basic formulation. In general, Eulerian models contain computational grid cells, while Lagrangian models are grid-free.

Eulerian models solve the three-dimensional advection-diffusion equation in a fixed grid, including the contribution of various physical and chemical sources and sinks, e.g., Shir and Shieh (1974) numerically integrated the following:

$$\frac{\partial C}{\partial t} = -\nabla \cdot \vec{V}C + \nabla \cdot K \nabla C + \tilde{Q} - k_0 C, \qquad (1)$$

where all symbols are defined in Appendix A.

The wind field and vertical eddy diffusivities in such a model could be provided by either interpolated meteorological observations, analytical formulations, or planetary boundary layer (PBL) model output. All Eulerian models solve some variation of the above equation, although they may differ in their initial conditions, spatial resolutions, boundary conditions, numerical techniques, simplifying assumptions, and/or turbulence parameterizations.

Emissions in Lagrangian models are represented by discrete elements (dimensionless points or volumes) transported by the mean wind and diffused by its turbulent component. Point type Langrangian models use particle in cell (PIC) or Monte Carlo methods, while volume approaches use puff techniques.

The PIC model of Lange (1973,1978) combined the advective and diffusive fluxes to produce the following form of (1):

$$\frac{\partial C}{\partial t} = -\nabla \cdot \left[C\left(\vec{V} - \frac{K}{C} \nabla C\right)\right]. \qquad (2)$$

As the second term in the parenthesis has the dimensions of velocity (i.e., a downgradient "diffusive" velocity), Lange defined a "pseudotransport velocity" $\vec{V}_p$ by

$$\vec{V}_p \equiv \vec{V} - (K/C)\,\nabla C\,. \qquad (3)$$

Particles thus disperse with a $\vec{V}_p$ composed of transport and diffusive components.

Although the PIC technique is Langrangian, it also has an Eulerian aspect, because a grid must be established and the particle sum in each cell is used to determine the concentration gradient in (3). It is convenient to use eddy diffusivity coefficients produced by PBL models, but the limitations of gradient transport (i.e., K) theory remain in PIC models.

Monte Carlo particle dispersion models avoid the K-theory limitations, as each of its particles move independently (Watson and Barr, 1976; Hanna, 1981). Dispersion results from the ensemble movement of a large number of particles, each moving with a velocity composed of the following: transport by a mean fluid velocity $\vec{\bar{V}}$, semi-random (but correlated) turbulent wind motions $\vec{V}'$, and completely random molecular diffusion $\vec{V}''$.

Zannetti (1981a,b) calculated the semi-random turbulent fluctuations $\vec{V}'$, auto- correlated for all three components and cross-correlated only between the vertical and along-wind directions, from

$$\begin{aligned} u'(t+\Delta t) &= R_x\, u'(t) + u''(t+\Delta t) \\ v'(t+\Delta t) &= R_y\, v'(t) + v''(t+\Delta t) \\ w'(t+\Delta t) &= R_z\, w'(t) + R_{xz}\, u'(t) + w''(t+\Delta t)\ . \end{aligned}$$

The auto and cross correlation coefficients (R_x, R_y, R_z, and R_{xz}) are functions only of a time interval Δt, and are assumed to decay exponentially as

$$R(\Delta t) = \exp\left(-\Delta t / T_L\right) .$$

The Lagrangian turbulent time constant T_L can be related to PBL parameters, such as wind speed and stability. The purely random components $\vec{V}''$ are assumed Gaussian, with their standard deviations given by

$$\sigma_{V''} = \sigma_{V'}\left[1 - R^2(\Delta t)\right]^{1/2},$$

where $\sigma_{V'}$ is a function of Monin-Obukhov length and friction velocity; see McNider et al (1980) for details.

While other dispersion modeling techniques require meteorological input not directly measurable (e.g., K's), Monte Carlo methods require only statistics directly obtainable from measurable velocity quantities. Nevertheless, investigation is still required to determine the correct methods to relate Eulerian wind measurements to the required Lagrangian statistics.

Volume elements, such as segmented plumes or puffs, are effective for the simulation of plumes from major point sources in time and space-varying windfields, because the technique is less computer intensive than other Lagrangian techniques, as fewer elements are required.

Segmented plumes are composed of continuous pieces, each of which represents emissions over a specific time period (Bass, 1980). The center point of each segment is advected with the prevailing local wind.

Within each segment, pollutants are assumed distributed with the following standard two-dimensional Gaussian cross section (Benkley and

Bass, 1979):

$$C = \frac{Q_e}{2\pi\,\sigma_y\,\sigma_z\,\bar{u}} \exp\left\{-\frac{1}{2}\frac{y^2}{\sigma_y^2}\right\} \cdot \left[\exp\left\{-\frac{1}{2}\frac{(z-H)^2}{\sigma_z^2}\right\} + \exp\left\{-\frac{1}{2}\frac{(z+H)^2}{\sigma_z^2}\right\}\right] . \qquad (4)$$

In all Gaussian equations, the x-axis is assumed oriented in the direction of the mean wind, and the origin of the coordinate system is at the stack base. The standard deviations of pollutant mass σ_y and σ_z are functions of total elapsed travel time or distance. Since they are also functions of turbulence along their trajectory, growth rates vary between segments.

Segmented plume models work best with uniform winds, which produce a nearly straight plume. Wind fields with considerable shear and/or time variability produce segmented plumes with sharp turns. Under such circumstances, pollutant mass is not conserved unless considerable computational time is devoted to treating the "elbows."

The second type of volume-element model approximates a continuous source with a series of discrete puffs advected by the local prevailing wind. Moving puffs, like plume segments, grow at rates proportional to local turbulent levels. Three-dimensional puff concentrations are usually assumed Gaussian, as follows:

$$C = \frac{Q}{(2\pi)^{3/2}\,\sigma_x\,\sigma_y\,\sigma_z} \exp\left\{-\frac{1}{2}\left[\frac{(x-\bar{u}t)^2}{\sigma_x^2} + \frac{y^2}{\sigma_y^2}\right]\right\} \cdot \left[\exp\left\{-\frac{1}{2}\frac{(z-H)^2}{\sigma_z^2}\right\} + \exp\left\{-\frac{1}{2}\frac{(z+H)^2}{\sigma_z^2}\right\}\right] . \qquad (5)$$

Puff models tend to produce symmetric concentration distributions, as they cannot simulate the effects of wind shear on scales smaller than their dimensions. A puff model capable of simulating the dispersive effects of such

shear was proposed by Sheih (1978); its concentration distribution is given by

$$C = \frac{Q}{(2\pi)^{3/2} L_x L_y L_z} \exp\left\{-\frac{1}{2}\left[\left(x - \bar{u}t - \frac{\zeta_7}{\sigma_z} z\right)^2 \sigma_x^{-2} + \left(y - \frac{\zeta_8}{\sigma_x} z\right)^2 \sigma_y^{-2}\right]\right\} \cdot \left[\exp\left\{-\frac{1}{2}\frac{(z-H)^2}{\sigma_z^2}\right\} + \exp\left\{-\frac{1}{2}\frac{(z+H)^2}{\sigma_z^2}\right\}\right]. \quad (6)$$

The modified diffusion coefficients (L's) are given in Shieh as complex algebraic combinations of the distances (ζ's) and angles in Fig. 1.

While the model is good for simulating plume behavior in wind fields with horizontal and vertical shear, it has shortcomings. First, it requires relatively complicated calculations associated with its geometric and trigonometric relationships. Second, it assumes that wind shear is equally important in all three dimensions; however, numerous field observations (e.g., Pooler and Niemeyer, 1970; Uthe et al, 1980) have shown that vertical gradients of wind and turbulence are the most important causes of plume distortion.

The Lagrangian Adaptive Volume Plume Model (AVP) of Ludwig et al (1989) approximates a continuous plume by a series of discrete volumes that change shape in response to vertical wind shear and changes of atmospheric stability with height (Fig.2). Each volume is described by five Lagrangian points at different altitudes. Horizontal and temporal changes in meteorological parameters are accounted for as the five points move and diffuse independently according to local meteorological conditions along their trajectories; thus each adaptive volume element consists of four segmented parts.

The mass continuity problems associated with the segmented plume model are avoided in the AVP model because it tracks the movement of segment edges and not their centers. At any given time meteorological effects are assumed uniform in any horizontal plane within the area encompassed by the adaptive volume.

Each volume has the following distribution of concentration:

$$C = \frac{Q}{(2\pi)^{3/2}\sigma_h^2\sigma_z} \exp\left[-\frac{1}{2}\left(\frac{s}{\sigma_h}\right)^2\right] \exp\left(-\frac{\tilde{z}^2}{2}\right), \tag{7}$$

where σ_y and σ_x have been assumed equal to an horizontally isotropic value of σ_h, and thus where horizontal concentration is a function of horizontal distances from the puff center. The dimensionless height $\tilde{z}$ is the number of "equivalent" standard deviations between the center of the adaptive volume and height z as follows:

$$\tilde{z}(z) = \int_{z_0}^{z} \frac{d\eta}{\sigma_z(\eta)}. \tag{8}$$

Ludwig et al (1989) tested the model with the following one-dimensional (vertical) inputs: steady-state uniform meteorological conditions--for comparisons with analytical solutions; "synthetic" meteorological inputs--to determine model responses to specified wind shear and fumigation situations; and observed meteorological inputs obtained near the Kincaid (Illinois) power plant--for comparisons with Lidar vertical plume sections (of relative concentration). These last simulations required concentrations on a computational grid in a vertical plane oriented perpendicular to the mean wind; grid locations thus had to be input for each simulation.

Results agreed with accepted steady-state analytical values, except near the stack, where (because of their sharp edges at $2\sigma_z$) adaptive volumes do not immediately produce the non- zero surface concentrations found with the standard Gaussian model. The model also generally reproduced plume dimensions, including complicated shapes produced by vertical wind shear. Simulated plumes were not always positioned correctly, but this would improve with wind fields more detailed than a single wind profile at the source.

Use of Lagrangian volumes that adapt their shapes to account for meteorological effects allows for the maximum use of spatial and temporal variations of meteorological conditions. This is achieved, however, with a nearly five-fold increase in computational requirements over usual puff approaches, but still considerably below those of similarly detailed Eulerian or PIC alternatives.

Advanced applications of three-dimensional (Eulerian or Lagrangian) dispersion models involve linkage with three-dimensional Eulerian PBL meteorological models. Such linkages allow for the simulation of pollutant dispersion under complex meteorological conditions. One such linkage was accomplished by Bornstein and Runca (1977), who studied the sea breeze effects on sulfur dioxide concentrations in Venice, Italy with a two-dimensional version of the URBMET PBL model linked to a Eulerian K-theory dispersion model. A later New York City (NYC) application by Bornstein et al (1987a,b,c) linked a three-dimensional version of URBMET with the three-dimensional Eulerian dispersion model of Shir and Shieh (1974). The PBL model provided the velocity and vertical diffusivity fields.

Results demonstrated that the linked models could correctly simulate most of the features of the time-varying polluted coastal urban boundary layer over NYC during sea breeze flow conditions.

One limitation in Bornstein et al (1987a,b,c) was the treatment of near-stack dispersion from large point sources, a general problem for Eulerian air quality models. The problem results from the limited spatial resolution of such models. Large plumes initially occupy a volume much smaller than the size of one dispersion model grid cell, and do not expand to fill a cell until downwind travel distances of at least several kilometers.

To resolve the discrepancy between the resolution possible in Eulerian air quality models and the characteristics of strong localized emissions, techniques must be developed to represent subgrid dispersion processes. One of the few models accomplishing the required linkage of scale is the Plume-Airshed Reactive Interacting System (PARIS) Model developed by Seigneur et al (1983), which embedded a Lagrangian plume model in the Eulerian SAI photochemical airshed model. Application of PARIS to St. Louis and Los Angeles showed the importance of including a detailed description of point source dispersion.

The adaptive volume plume model is effective in describing pollutant dispersion processes before they can be adequately treated within the cells of a Eulerian model. The formulation of Ludwig et al (1989), however, requires user specification of the points at which concentration is to be calculated. This is somewhat restrictive for general use, when pollutants may be transported in any direction. To make the model more useful, the current study developed a moveable fine mesh grid based on pollutant location at

each time step in a complex meteorological field. While the previous application of the AVP model only computed concentrations in pre-selected vertical planes, the current application conducted a detailed evaluation of the effect of various surface boundary conditions on predicted surface concentrations. The modifications and the improved understanding will facilitate the ultimate incorporation of the AVP Model into the linked Eulerian PBL and urban dispersion models used in the NYC coastal urban boundary layer study.

2. METHOD

The original Lagrangian AVP Model of Ludwig et al (1989) constructed its concentration computational-grid before each simulation. In the current study, the model has been modified to construct a grid based on an initial estimate of pollutant location. This involved several difficulties, e.g., determining locations of the pollutant center of mass and estimating the computational domain edges. These tasks can be complicated with complex meteorological conditions, such as wind shear or stability changes with height and/or time.

a. Original model

The AVP Model approximates a continuous plume by a series of discrete volumes that change shape in response to vertical (speed and/or direction) wind shear and changes of atmospheric stability with height. Each adaptive volume is characterized by five points at different altitudes and five associated horizontal radii (Fig. 2). Pollutants in each adaptive volume lie between the lowest and highest points, thus defining the fraction of material in a given layer of thickness Δz by the following piece-wise Gaussian function

$$q = \frac{\Delta z}{2\pi \sigma_z} \exp\left(-\frac{\tilde{z}^2}{2}\right), \tag{9}$$

where $\tilde{z}$ is defined by (8). The term "equivalent" in the definition of $\tilde{z}$ equates the amount of material between the middle point of the volume z_0 and the altitude corresponding to $\tilde{z}$ with the material found between the mean and a point $\tilde{z}$ standard deviations from it in the usual Gaussian distribution. Use of $\tilde{z}$ removes σ_z from the denominator of the exponential term in (7). With a uniform with height σ_z, (7) reduces to the usual Gaussian form.

Figure 2 shows that σ_h varies with height, and that the separation of the five points in each adaptive volume defines four independent σ_z values. A constant σ_z is assumed between adjacent vertical points, so that $\tilde{z}$ varies linearly with height. The values of σ_h are linearly interpolated with height between the values at the five points. Each Lagrangian volume is assumed to extend radially to $3\sigma_h$ from the volume centerline (horizontal broken lines in Fig. 2). Material more than $2\sigma_z$ above or below the center point, or horizontally more than $3\sigma_h$ from the centerline, amounts to less than five percent of the total and is ignored. As seen below, this sometimes produces anomalous behavior.

Every 10 minutes, a group of N adaptive Lagrangian volumes, each containing the same mass, is generated. The number released depends on local wind speed and turbulent diffusion at the source, i.e., N is chosen so that the space between the first two volumes released during any period will approximately equal σ_h /2 at the end of that period. The first volume travels for the entire ten minutes, the next travels a fraction [(N-1)/N] of the period, etc. The five points defining the shape of any one volume are initially aligned vertically, with a separation (σ_z) of 3 m; this accounts for the initial finite dimension of large sources. Model results are generally insensitive to this value.

The horizontal motion of each of the five points in one adaptive volume is calculated using spatially interpolated meteorological conditions at two-minute time-steps. Vertical advection (Fig. 2) arises from the sum of the specified vertical air motion $\overline{w}$, calculated rate of plume rise w_p (as discussed in Ludwig et al, 1989), and vertical diffusion velocity w_d. To calculate w_d, the

model incorporates the parameterization of Ludwig et al (1977) for σ_z in terms of both the horizontal travel distance d of each of the five points defining an adaptive volume and Pasquill-Gifford stability class j as follows:

$$\sigma_z (d,j) = \alpha_j d^{\beta_j} . \qquad (10)$$

The derivative of (10) with respect to d is used to obtain w_d as follows:

$$(w_d)_i = -V_h \left(\frac{\partial \sigma_z}{\partial d} \right)_i , \qquad i \neq 3 .$$

The effects of the expansion of the inner portions of the volume were treated incorrectly in the original version of the model. The outer most points should reflect the sum of the expansion of the two sections between them and the center point. Originally the rate of the expansion of the outer parts of the volume were simply doubled, as though the two were expanding at the same rate.

Once the five total w_i values are determined, new center point heights are obtained for each of the five adaptive volume segments. The height difference between any two adjacent center points becomes one of the four final σ_z values for each volume at each time step. Unless constrained, the vertical separation between adjacent points within one volume could decrease, tantamount to "negative diffusion," so the model prohibits each outer point from moving away from the central point more slowly than its corresponding inner point. The horizontal diffusion coefficients σ_h at the five points are also functions (via Ludwig et al, 1977) of the total horizontal travel distance of its corresponding point, i.e.,

$$\sigma_h(d,j) = \lambda_j d^{0.9} . \qquad (11)$$

Values obtained from (10) and (11) approximate the Turner (1970) diffusion curves.

It is commonly assumed that plumes interact with an underlying surface in a manner analogous to the reflection of light. The "reflected" plume component is often treated by assuming a virtual source mirrored below the reflecting surface (Fig. 3). In AVP models, this is accomplished by allowing for negative z values, but by advecting and diffusing according to conditions at the corresponding absolute values of z.

Ludwig et al (1977) achieved computational efficiency by merging overlapping elements separated at all levels by σ_h or less. The five points of the merged volume are assigned coordinates and parameters averaged from those in the two original volumes.

Volumes are removed from further consideration when their five points move outside the modeling domain. When only some are outside, meteorological variables at the nearest grid point within the domain are used. This approach could cause problems with wind reversals that would otherwise bring volumes back into the domain.

Up to 100 arbitrary locations (receptors), where concentration is to be calculated, must be specified at each time step. The model rank orders these so that it considers only those "near" (within approximately $3\sigma_h$) an adaptive volume. Concentrations are calculated at specified time intervals by summing concentrations obtained from (7) over all adaptive volumes. Ludwig et al (1989) give additional details.

b. Modified model

The main modifications made to the AVP model involve techniques

developed to locate systematically (at each time step) a previously emitted plume or puff. These locations are used to establish a fine mesh concentration computational grid. Definition of the grid requires several steps, including determination of an estimate of the "absolute" concentration field based on a "relative" concentration field.

In the first step, the six "extreme positional points" of the ensemble of all the various sets of five center points of each Lagrangian volume constituting the puff or plume are located. These six points include those with the largest and smallest x-direction coordinates (in the meteorological grid), as well as those with the largest and smallest y-and z-coordinates (Fig. 4).

These points are used to identify a volume that contains "most" of the pollutant mass (Fig. 4). The upper and lower vertical extents of the volume are given by the maximum and minimum (above the surface) vertical positional points, respectively. The volume is then divided into 25 by 25 by 10 (vertical) sub-volumes.

An approximate concentration is calculated for each cell by taking a weighted sum of all points within that cell. The weight F assigned each point is approximately proportional to the mass associated with it and is defined by

$$F = \frac{f(\sigma_z)}{\sigma_h^2},$$

where σ values are those associated with the point and f is the value of the Gaussian normal function at 0, 1, or 2σ from the mean, i.e., 1.0, 0.37, and 0.13, respectively. The relative concentration for a grid cell is than the sum of the weights associated with each point within it.

After the sub-volume with the maximum relative concentration is identified, and the program searches in the N, S, E, W, up, and down directions to find the extreme sub-volume in each direction containing a relative concentration that equals or exceeds a specified fraction of the maximum value. For the current simulations, that fraction has been taken as 0.1. The resulting volume, constructed with outer edges that coincide with the appropriate outer edges of the above identified six computational sub-volumes, contains most of the pollutant mass. The points of adaptive volumes within this new volume are used to define the final volume in which absolute concentration will be calculated. The procedure for this is that used in the calculation of relative concentration (Fig. 4), except that a value of 4σ is used (instead of 3σ). This produces aesthetic contour plots, whose outer isopleths tend to define the "edge" of the pollutant mass.

The final volume is then divided into a grid containing 10 by 10 by 10 points, the outer of which are on its boundaries. The (final absolute) concentration at each of these grid point is calculated by summing all concentrations obtained from (7). The entire procedure (including both the relative and absolute concentration phases) is repeated to calculate surface concentrations in the region (if any) where the puff or plume has intersected the surface. A Δz of 10 m is used for the relative concentration phase of this calculation, but the final absolute concentration is not effected by this choice.

For instantaneous (puff) sources, the model produces isopleth concentration distributions in horizontal planes located at the surface and at the effective stack height level. Vertical (x-z and y-z) output planes are also constructed through the location of the absolute maximum concentration.

For continuous (plume) sources, the same horizontal planes are produced, but vertical planes are constructed through the downwind midpoint of the plume.

3. RESULTS

The Adaptive Volume Plume (AVP) Model uses the following meteorological input data at each 10 min timestep for each meteorological grid point (from observations or from PBL model output): wind components ($\bar{u}$, $\bar{v}$, and $\bar{w}$) for advection and ambient air temperatures (T). The latter are used to evaluate grid point vertical temperature gradient values, which in turn are related to grid point Pasquill-Gifford stability class (Table 1) and to the constants used to calculate σ_h and σ_z via (10) and (11), respectively. Normally, the model also requires the following source characteristics for plume rise calculations: exit temperature and velocity; pollutant emission rate (Q); stack location (x_0, y_0, h), and stack diameter.

The current study only considers a specified constant prescribed effective stack height (for ease of comparison with analytical Gaussian solutions), so some source parameters need not be specified. The following constant source information was specified for all simulations presented here: $x_0 = 100$m, $y_0 = 2.5$ km, $Q = 4.8$ kg s^{-1}, and $H = 250$m.

Case a. Steady-state uniform meteorology

An arbitrary specified uniform steady-state wind with a westerly flow of 0.4 ms^{-1} was specified for an "short term" (10 min) release of a single adaptive volume into a moderately unstable (Class B) temperature profile (Υ=1.8°C/100m); results were compared with analytical Gaussian solutions given by (5), using σ_h and σ_z values approximated by (10) and (11),

Table 1

LAPSE RATE/STABILITY RELATIONSHIPS
(from Ludwig et al, 1989)

Stability Description	Stability Class	$\partial T/\partial z$ (°C/100m)	Constants for Eqs. (10) and (11) α	γ	λ
Extremely unstable	A	<-1.9	0.025	1.38	0.428
Moderately unstable	B	-1.9 to -1.7	0.075	1.07	0.301
Slightly unstable	C	-1.7 to -1.5	0.112	0.91	0.198
Neutral	D	-1.5 to -0.5	0.196	0.72	0.128
Slightly stable	E	-0.5 to 1.5	0.231	0.64	0.095
Moderately stable	F	1.5 to 4.0	0.227	0.575	0.065

respectively. A low wind speed was chosen, as such conditions are difficult for finite-difference Eulerian models to simulate, and the AVP Model will ultimately be embedded in such a model.

The advection and relatively rapid diffusive growth of the puff during its earliest 160 min of travel (Fig. 5) under the westerly flow conditions reflects the fairly high turbulence levels associated with Pasquill-Gifford Class B stability conditions. Concentration distributions after 60 min of travel time are shown in Figs. 6 and 7 for horizontal planes at H and at the surface, respectively. Because there is no shear, the puff has a vertical axis, and so both distributions have the expected radially symmetric concentration patterns, centered at the same x-y position. Surface concentration values are smaller than those at H, although surface reflection is already underway.

Vertical concentration cross sections along the downwind puff axis show that reflection, not strong after 30 min of travel (Fig. 8), is quite apparent

after 60 min (Fig. 9). The latter section shows that mixing and reflection move the maximum concentration towards the surface.

After 110 min (not shown) the puff has expanded, causing concentrations at both stack height and the surface to decrease. The lack of shear causes horizontal concentration distributions to remain symmetric, but as the polluted layer becomes deeper and better mixed (Fig. 10), the vertical concentration gradient reverses. Values thus decrease with height due to upward reflection from the surface. After more time, continued reflection reduces the vertical concentration gradient to near zero throughout.

The decrease of (Lagrangian) concentration as the puff moves downwind at the concentration computational-grid point (at each time step) closest to its center is seen in Fig. 11. The initial rapid decrease of concentration by diffusion is later slowed by the upward diffusion of mass via surface reflection.

Concentration values at the ground directly beneath the moving puff are, of course, lower than those at H (Fig. 12). They first rise as the volume diffuses to the surface and then fall as the moving puff continues to expand and material disperses through a larger volume. The first four non-zero AVP model concentrations in Fig.12 are obtained from the spatial concentration distribution computed at the 50 min time step, when the bottom edge of the puff first reflects off the ground.

Comparison of Lagrangian AVP surface concentration values with those from the analytical solution given by (5) shows exact agreement beyond the 1 km distance (Fig. 12). The lack of agreement near the stack arises because AVP puffs only extend $\pm 2\,\sigma_z$ vertically about its center point. A puff

thus does not contribute to surface concentrations until σ_z exceeds half the centerpoint height.

After 40 min of travel (0.97 km), the bottom edge of the simulated puff for this case is 6 m above the surface where the concentration (according to the standard normal distribution) is 13.5% of the center point value. At the surface (corresponding to 2.06 σ_z) the AVP model still gives a zero concentration, compared to the analytical (standard normal) gaussian solution that yields a value of 12% of the center point value without reflection and 24% with the reflection term in (5). One time step later at 1.2 km downwind), the puff has reached the surface and reflected to a height of 55 m, so that this and subsequent surface concentrations agree exactly with the analytical solution.

The first non-zero AVP surface concentration in Fig. 12 is also its peak value. This will not always be the case, but the first non- zero surface concentration will generally be a large fraction of its peak value, unless the concentration calculation time step is reduced below its current 10 min value.

Comparison of Lagrangian AVP and Gaussian solutions at H (Fig. 11) shows Gaussian values near the stack ever so slightly higher than corresponding AVP values, because the Gaussian model includes surface reflection effects at all times, while AVP results do not include them before the bottom of the adaptive volume touches the surface. After AVP reflection, exact agreement is expected from the surface up to the $2\sigma_z$ upper edge of the image puff. Above this level, the AVP model still produces slightly lower concentrations than the Gaussian model. This effect is seen at H during the first 2 km of travel distance, as it took between 70 and 80 min of travel time

for the $2\sigma_z$ image puff edge to pass upwards beyond H.

Concentration calculations in an Eulerian framework at fixed site No. 1 in Fig. 5, which is 1.55 km downwind and within 60 m of the centerline, are shown for the surface and aloft at H/2 and H in Figs. 13-15, respectively. The puff has a cylindrical shape for this case. Nonzero concentrations are observed at all levels after 40 min. As the puff passes, concentrations rise and fall in unison because of the vertical orientation of the cylindrical volume.

This site is close enough to the source so that mixing has not eliminated the concentration decrease with height (Fig. 16a). Further downwind, at 2.5 and 4.7 km (sites 2 and 3 in Fig. 5), surface reflection (Figs. 16b and c, respectively) reverses the gradient (as discussed above). At the final site (6.1 km downwind, not shown in Fig. 5), the polluted layer has become almost completely mixed. Peak concentrations decrease and the time period for passage increases with downwind distance due to diffusion. Note that peak centerpoint and surface concentrations are somewhat less at the fixed sites than at the corresponding (same time step) Lagrangian values given earlier. This is because the Eulerian points were 60 m from the vertical axis through the puff center of mass (Fig. 5) when concentrations were calculated.

Comparison of the surface analytical Gaussian and AVP results at the site 1.55 km east (downwind) of the source shows exact agreement after 40 minutes (Fig. 13), i.e., after the AVP puff touches the ground. At 40 min, the AVP value is zero, because the point used for the comparison was beyond the $3\sigma_h$ horizontal edge of the AVP puff, but in a region of small Gaussian concentration that exists because of the infinite extent of the Gaussian formulation.

Comparison of the analytical Gaussian and AVP results at H/2 shows exact agreement (Fig. 14) after 50 minutes of travel, i.e., when the $2\sigma_z$ image source reflected puff edge passes this level. Before this, the AVP model slightly underestimates Gaussian results. The same pattern is found at H (Fig. 15), except that the $2\sigma_z$ image source puff edge does not pass this level until after 70 minutes. At all levels, the concentration underestimate produced by the AVP model is a maximum at the time proceeding passage of the $2\sigma_z$ image source edge. This is true, as the non-zero value of the reflected Gaussian component value increases with each time step, while AVP values remain zero until the reflected point reaches the level where concentrations are being calculated.

In principle, the sharp edge of the AVP model at $2\sigma_z$ is physically more realistic than the infinite diffusion speed associated with the Gaussian model. However, the abrupt discontinuity associated with truncation at $2\sigma_z$ suggests that the vertical extent of the volumes should be expanded to at least $3\sigma_z$. With this, only 0.3% of the total puff mass (rather than the current 4.5%) would be excluded. At $3\sigma_z$ the concentration is only 1.1% of the centerpoint value (the current is 13.5%), and the resulting maximum concentration difference between the analytical and AVP values at the surface would then be 2.2 %, rather than 27%.

Case b. Speed shear

To study the effect of a speed shear with height, the $\bar{u}$ component of an Ekman profile was specified (Fig. 17) by the following:

$$\bar{u}=u_g\,(1-e^{-az}\cos az) \quad , \qquad (12)$$

where

$$a = \sqrt{\frac{2\,\Omega \sin \phi}{2\,K}} \quad . \tag{13}$$

The above equations were solved for the K-value that would produce a speed of 0.4 ms^{-1} at H, as in Case a. With input values of u_g =2ms^{-1} and ϕ = 45°, K = 79 $m^2\,s^{-1}$. All other input parameters were identical to those of Case a. Note that $\overline{v}(z)$ is ignored for this speed-shear only case.

The advection and diffusive growth of each of the four segments of the adaptive volume after 40 minutes travel (Fig. 18) reflects the effects of the specified speed shear. The puff axis is no longer vertical, but curved and tilted downstream with height. While the middle point of the puff advects at the same rate as in Case a, the shear now causes the upper segments to move faster, and as σ is dependent on d, to diffuse more rapidly than the lower two segments. If a more realistic stability stratification was used, so that turbulent diffusion proceded more slowly aloft, away from the heated surface, this effect would not be so pronounced. The upwind displacement of the upper two center points relative to the tilted dashed line that represents constant shear results from the less than linear nature of the shear produced by an Ekman spiral.

The spatial distribution of concentration at Level H (not shown), is still radially symmetric, but magnitudes are lower than corresponding values from Case a (Fig. 19). The shear moves each of the five points defining the puff with a different speed, so that the equal values of σ_z in the uniform wind case are replaced by values that increase with height. The computer code calculates concentrations at the height of the three internal points (including

the one at H) using the σ_z value for the puff segment above it. Concentrations at H for Case b are less than those of Case a, because the point above H has traveled further, so its σ_z is larger. The code should be changed to use an average of the σ_z values in the segments immediately above and below the three internal segment boundaries. Since the increase of the σ_z value above the center point is larger than decrease of the σ_z value below, the sum of the volumes immediately above and below the center point would still be greater than for Case a, causing concentration values at H to be smaller, but by a lesser amount.

Note that the current net increase (relative to Case a) in the volume surrounding the puff centerpoint arises from the power law relationship of $\sigma(d)$. A linear or weaker relationship, in conjunction with the current less than linear wind profile, would produce opposite results, i.e., a net decrease in volume size and an increase in concentration (both relative to Case a). Only stability classes in Table 1 with a value of γ greater than unity (i.e., A and B) produce a decrease in concentration relative to the uniform wind case in conjunction with a less than linear wind shear.

If σ -values depended on travel time, rather than travel distance, then σ_z -values would always be uniform with height, as long as stability was uniform with height, because the travel times for all points in an adaptive volume are the same. Before the effects of surface reflection, the two segment volumes above H would thus decrease in size (relative to their current Case b sizes), while the two below would grow. Concentrations above H would therefore increase, while those below H would decrease. With any (non-linear or linear) speed shear, this change would produce a vertically uniform

(before reflection) Case b concentration field, with values identical to those of Case a (because the puff segments of Case a would be uniform and equal to those of Case b).

Surface concentrations directly under the Lagrangian moving center point of the puff are zero, unlike those of Case a, because the lower two points of the puff now lag well behind the center point. When they hit the ground, they still produce a symmetric concentration pattern, but well upwind of the location in Case a. This produces higher concentrations than those of Case a because of the travel distance dependence of σ_h and σ_z.

With the (usual) non-slip (V=0) surface boundary condition, the model behaves unrealistically. As the lower edge of the puff nears the surface, its horizontal speed approaches zero, so that the vertical diffusion velocities also approach zero. This causes the upward reflection (by diffusion) to be delayed. In fact, if a time step coincides with the arrival of the bottom point at the surface, its motion will be forever halted.

While wind shear produces a downstream (longitudinally) tilted puff with a peak concentration at H (Fig. 20), the boundary problem discussed above ultimately creates an erroneous peak concentration (before surface reflection) below H (Fig. 21). The vertical gradient from this erroneous maximum concentration is larger downward than upward, as concentration normally increases towards H. This boundary problem is also experienced in PIC and Monte Carlo type Lagrangian models (Zannetti, 1981a,b). A time-dependent σ_z formulation would correct the artifact discussed above.

Lateral concentration cross sections (not shown) for Case b show the expected lateral symmetry. They also show the non- symmetric vertical

gradient discussed above.

Case c. Directional shear

To produce a directional shear with height, the $\bar{v}$ component of the Ekman spiral of Case b was evaluated (Fig. 17) as follows:

$$\bar{v} = u_g e^{-az} \sin az .$$

All other input parameters are again identical to those of Case a, including a uniform u-component.

The effects of the specified steady-state lateral speed is reflected by the linearly increasing lateral displacement (Fig. 22) during its first 160 minutes of travel at the puff center point from the dashed- line trajectory of Case a.

All concentration values for Case c (before effects of surface reflection) at any given travel time are less than those of Case a, because the total horizontal travel distance of the puff center is increased by the lateral displacement. Increased travel distance increases both σ_h and σ_z, thus producing the lower concentrations and producing an earlier surface impaction (almost 40 versus almost 50 min).

While concentration patterns (not shown) are still symmetric in the horizontal (as in Cases a and b) and longitudinal planes (as in Case a), the directional shear produces a tilted (in the direction of the $\bar{v}$ -component of the flow) vertical puff axis. After 40 minutes, the peak concentration is at H, when the puff first impacts the surface (Fig. 23) After 60 min, the peak concentration has moved to the surface (Fig. 24), due to initiation of the well mixed layer (as in Case a). In this case, however, the layer forms earlier because of due to the increased travel distance.

Comparison of Lagrangian concentrations computed at the grid point closest to the center of the moving middle segment of the puff shows values less than those of Case a, because of the increased travel effect discussed above (Fig. 19). Concentrations with directional shear could be either higher or lower than those with speed shear, depending on the magnitude of each shear. With the shear values of Cases b and c, the direction-shear influenced concentration values are first less than and then greater than the speed-shear influenced values at $\bar{H}$ (Fig. 19). The cross-over occurs about 2 km east of the source.

Comparison of surface concentrations under the moving middle segment of the puff (Fig. 25) shows surface impaction earlier in Case c than in Case a, because of the larger travel distance associated with the lateral displacement. These Case c surface concentrations are less than those in Case a, because the lower two segments laterally displace more slowly than does the center segment. These Case c surface concentrations are thus evaluated only in the low concentration region at the lateral edge of the lowest puff segment.

Case d. Subsidence velocity

The effects of subsidence on a dispersing puff have been studied by specifying vertical wind components that vary linearly with height (Fig. 26). All other variables are again identical to those of Case a.

The nonlinear subsidence of the puff center point (Fig. 27) is a combination of the constant $\bar{u}$ and the linearly decreasing $\overline{w}(z)$, as the point approaches the surface. The puff, of course, hits the ground earlier than in

Case a (within 40 rather than 50 min). The concentration distribution (not shown) in both the horizontal and vertical planes through the puff center is symmetric before surface reflection, as in Case a, but concentrations are greater. The decreasing subsidence with height compresses the volumes of the four puff segments unequally as they sink to the surface. Subsidence produces a well mixed pollutant layer before it appears in Case a, because surface reflection is initiated earlier. Surface concentrations, and those at the level of the maximum, are both higher after 60 minutes in Case d (Fig. 28) than in Case a (Fig. 9) for the reasons cited above.

Computed concentrations at height H at the x-y grid point closest to the center point of the moving puff shows that near the stack, Case d values are less than those of Case a, because subsidence lowers the center point and reduces concentrations at H. By 2.3 km, concentrations at H for Case d are higher than those in Case a, because of the non-linear nature of the subsidence, which again unequally compresses the volume of each of the four puff segments as they rise upwards to H. This more than compensates for the retarding nature of the subsidence, which delays the passage past H of the $2\sigma_z$ edge of the image source. This retardation would tend to reduce Case d concentrations below those of Case a. Non-zero surface concentration values in Case d occur earlier and are greater than those of Case a (Fig. 25), again due to the subsidence.

Case e. Fumigation

Fumigation conditions were investigated by creating a growing layer of depth $h_c(t)$ in which the Pasquill-Gifford stability class B conditions of the previous cases were replaced by class A conditions. The change was initiated

after 20 minutes (Fig. 29). The depth of the extremely unstable layer h_c increased uniformly 50 m every 10 minutes until reaching 250 m after 70 minutes. All other variables are identical to those of Case a.

The layer of stability class A reached to a height within the second lowest puff segment after 40 minutes (Fig. 30). While the upper two segments of the puff diffused (vertically and horizontally) at the same rate as in Case a, the lower two segments diffused more rapidly due to the changed stability.

During the first 30 minutes (i.e., before h_c grows deep enough to intercept the lower puff edge), Case e concentrations (not shown) are identical to those of Case a. Surface reflection occurs about 10 minutes earlier in Case e than in Case a, due to the more rapid spreading associated with the fumigation process (Fig. 25). Lagrangian surface concentrations under the moving puff center point are therefore initially higher for Case e than for Case a, but the enhanced mixing reverses the effect after 50 minutes (travel distance of 1.2 km).

Lagrangian concentrations (not shown) at the concentration computation grid point closest to the coordinate of the center of the moving puff are identical to those of Case a for the first 60 minutes (1.45 km). After this time, surface reflection effects reach H, and its concentrations (Fig. 19) exceed those of Case a for the next 20 minutes--until h_c reaches H. After 80 minutes (1.93 km), Case e concentrations are lower than those of Case a, because of the increased dilution accompanying fumigation.

As mentioned in the discussion of Case b, a formulation in which concentrations at H were dependent on σ_z-values in the volumes immediately above and below H (as opposed only to the one above) would

produce a fumigation related lowering of concentration beginning at 60 minutes, when h_c reached the meteorological grid point immediately below the second lowest of the five points defining the adaptive volume. This effect could also have reversed the higher Case e concentrations (relative to those of Case a) at at the 70 and 80 minutes time steps.

The Longitudinal axial concentration cross section at 60 minutes (Fig. 31) also shows that Case e concentrations are greater than those of Case a (Fig. 9). Figure 31 also shows the effects of fumigation on puff shape through its lowest 200 m. The cross section after 110 minutes (Fig. 32) likewise shows Case e concentrations to be less at H relative to those shown for Case a in Fig. 10. Fumigation also dispersed the peak concentrations found near the surface for Case a, producing peak concentrations are at H for Case e.

In general, the AVP model correctly simulates the effects of fumigation; however, a singularity in the model formulation results in discontinuities of predicted concentrations at the three interior model points. At any level between any two of the five points, σ_z is constant, while at either of the two boundary points, σ_z is equal to that at the adjacent volume segment; however, the AVP code arbitrarily sets the σ_z value for the three interior points equal to the value of the volume segment above it. As a result, fumigation does not affect (i.e. lower) the concentration at any of these three sites until h_c grows to their height.

This, however, is not as physically reasonable as using a value for these points that would be an average of the values immediately above and below the point. In such a case, concentrations at either of these three points would be affected by the fumigation when h_c grew to a height equal to the model

point below the level of interest. It would then increase the σ_z value below the level of interest, thus lowering concentrations earlier than with the current formulation.

4. CONCLUSION

The original Adaptive Volume Plume (AVP) model approximates a continuous plume by a series of discrete volumes that change their shape in response to vertical wind shear and changes of adaptive stability with height. While the concentration calculation-grid domain had to be input in the original AVP model, the modified model now systematically locates (at every time step) previously emitted pollutants and establishes a moveable fine mesh grid that encompasses the volume within which the pollutants are found.

The grid on which concentrations are calculated is defined in several steps, which involve determining an estimate of the "absolute" concentration field using a "relative" concentration field. The modified model was tested for an instantaneous (10 min) release producing a single puff, so that its behavior could be easily evaluated under various complex meteorological conditions. Use of a single puff uncovered several discontinuities that were obscured by the overlapping of the many puffs in the previous plume study of Ludwig et al (1989).

Model results underestimate steady-state analytical Gaussian results until the image source (reflected) edge at $2\sigma_z$ passes the calculation grid point. This is true in part because the model does not incorporate the infinite diffusion speed of the Gaussian model, but only calculates concentrations within a volume bounded by $\pm 3\sigma_h$ and $\pm 2\sigma_z$. While an infinite diffusion speed is not realistic, the current results have shown than the $\pm 2\sigma_z$ vertical boundaries ignore too large a fraction of the pollutant mass. The AVP model could thus be improved by arraying the five points arrayed differently, e.g.,

they could represent the 0, 1.5 and $3\sigma_z$ positions instead of the 0, 1, and 2 positions. Two additional points could be added to achieve the extension to $\pm 3\sigma_z$, but this would require additional computations.

It is also recognized that the modified model overestimates near-stack surface concentrations when the puff or plume edge approaches the surface with a non-slip (zero flow) boundary condition. The resulting lack of advection prevents pollutant dispersion, as the σ-formulation is dependent on travel distance. The problem could be eliminated by using a formulation dependent on travel time, not travel distance. Such a change would affect the puff distortion in vertical speed-shear cases that results from the travel distance formulation.

Complicated puff shapes caused by wind directional shear, subsidence, and fumigation conditions are generally well represented by the model. A singularity in the model formulation, however, results in discontinuities in predicted concentration values at the levels of the three interior model points (out of the five that define a single adaptive volume), because the AVP code arbitrarily sets the σ_z-value for the three interior points equal to the value of the volume segment above it. This can be corrected by using the average of the σ_z-values immediately above and below each of the three interior points.

One of the purposes in developing the adaptive volume concept was to provide a model that could fully use outputs from advanced PBL models. Improvements need to be made in the model before such a linkage can be achieved, e.g., the $2\sigma_z$ edge of the puff should be expanded to $3\sigma_z$. In addition, the σ-formulation should be based on travel time, not travel distance. Linkage of the model to an advanced PBL model would provide the

meteorological parameters (e.g. diffusivities or turbulent intensities) necessary to produce such a travel time formulation.

While the shortcomings of the model uncovered by this research are important, they should not be difficult to correct. Possible corrective measures have been suggested, and they should be implemented and tested before the model is linked to either a PBL or objective analysis wind model.

REFERENCES

Bass, A, 1980: Modeling long-range transport and diffusion, Proc. Second Joint Conf. on Applications of Air Pollution Meteorology. March 24 - 27, 1980, Boston, MA, American Meteor. Soc. and Air Pollut. Control Assoc., 193-215.

Benkley, C.W., and A. Bass, 1979: Development of mesoscale air quality models. Volume 2: user's guide to Mesoplume (mesoscale plume segment) model. Contract Report, National Oceanic and Atmospheric Administration, Contract 03-6-02-35254, Environmental Research and Technology, Concord Mass., 141 pp.

Bornstein, R.D., and E. Runca, 1977: Preliminary investigation of SO_2 patterns in Venice, Italy using linked PBL and K- models, including removal processes. Proc. Joint Conference on Applications of Air Pollution Meteorology. Nov. 22- Dec. 2, 1977, Salt Lake City, UT, American Meteor. Soc. and Air Poll. Contr. Assoc., 277-282.

Bornstein, R.D., S. Klotz, U. Pechinger, R. Salvador, R. Street, L.J. Shieh, F. Ludwig, and R. Miller, 1987a: Application of lined three-dimensional PBL and dispersion models to New York City. In Air Polluntion Modeling and Its Applications V, Plenum Press, New York, 543-564.

Bornstein, R. D., U. Pechinger, R. Miller, S. Klotz, and R. L. Street, 1987b: Modeling the polluted coastal urban environment. Volume 1: PBL model. EPRI Report EA-5091 for Contract No. 1630-13, 172 pp.

Bornstein, R.D. U. Pechinger, R. Salvador, L.J. Shieh, and F. Ludwig, 1987c: Modeling the polluted coastal urban environment. Volume 2: Dispersion Model. EPRI Report EA-5091 for Contract No. 1630-13, 153 pp.

Hanna, S.R., 1981: Langrangian and Eulerian time-scale relations in the daytime boundary Layer. J. Appl. Meteor., 20, 242-249.

Lange, R., 1973: ADPIC, a three-dimensional dispersal and deposition under complex conditions. Lawrence Livermore Laboratory Report UCRL-51462, TID 4500, UC-32, 60 pp.

Lange, R., 1978: ADPIC, A Three-dimensional particle-in-cell model for the dispersal of atmospheric pollutants and its comparison to regional tracer studies. J. Appl. Meteor., 17, 320-329.

Ludwig, F. L., R. Salvador, and R. Bornstein, 1989: An adaptive volume plume model. Atmos. Environ., 23, 127-138.

Ludwig, F. L., L. S. Gasiorek, and R. E. Ruff, 1977: Simplification of a Gaussian puff model for real-time minicomputer use. Atmos. Environ., 11, 431-436.

McNider, R.T., S.R. Hanna, and R.A. Pielke, 1980: Sub-grid scale plume dispersion in coarse resolution mesoscale models. Second Conference on Industrial Meteorology, New Orleans, LA., 424-429.

Pooler, F., and L.E. Niemeyer, 1970: Dispersion from tall stacks: an evaluation. Proceedings 2nd International Clean Air Congress, Academic Press, New York, 1049-1056.

Seigneur, D., T.W. Tesche, P.M. Roth, and M.K. Liu, 1983: On the treatment of point source emissions in urban air quality modeling. Atmos. Environ., 17, 1655-1676.

Sheih., C.M., 1978: A puff pollutant dispersion model with wind shear and dynamic plume rise, Atmos. Environ., 12, 1933-1938.

Shir, C.C., and L.J. Shieh, 1974: A generalized urban air pollution model and its application to the study of sulferdioxide distribution in the St. Louis metropolitan area. J. Appl. Meteor., 19, 185-204.

Turner D.B., 1970: Workbook of Atmospheric Dispersion Estimates. Environmental Protection Agency, Pub. No. AP-26, 84 pp.

Uthe, E. E., F.L. Ludwig, and F. Pooler., Jr. 1980: Lidar observations of the diurnal behavior of the Cumberland Power Plant Plume. J. Air Pollut. Control Assoc., 30, 889-893.

Watson, C.W., and S. Barr, 1976: Monte-Carlo simulation of the turbulent transport of airborne contaminants. Los Alamos Scientific Laboratory, Technical Report No. LA 6103, 73 pp.

Zannetti, P., 1981a: An improved puff algorithm for plume dispersion simulation. J. Appl. Meteor., 20, 1203-1211.

Zannetti, P., 1981b: Some aspects of Monte-Carlo type modeling of atmospheric turbulent diffusion. Conference on Probability and Statistics in Atmospheric Sciences, AMS, Monterey, CA Nov. 2-6, 1981.

APPENDIX A: LIST OF SYMBOLS

Roman Letters

C	concentration
d	horizontal travel distance
F	weighting function used in relative concentration calculation
f	weight used in relative concentration calculation
H	effective stack height
h	stack height
h_c	depth of very unstable layer
K	eddy diffusivity coefficient
k_0	Linear chemical reaction rate
L_m	diffusion coefficients for sheared puff model of Shieh
N	number of adaptive volumes released during 10 min interval
P_m	tracer particles defining sheared puff in model of Shieh
Q	mass in a volume
Q_e	mass emission rate
$\tilde{Q}$	concentration emission rate
q	fraction of total material in horizontal layer
R	correlation coefficient
s	horizontal distance from puff center point
t	time
T	environmental temperature
T_L	Lagrangian time constant
u,v,w	westerly, southerly, and upward wind components, respectively

$\vec{V}_p$	pseudotransport velocity
$\vec{V}$	total wind velocity
W	total vertical motion
w_d	vertical motion due to turbulent diffusion
w_p	vertical motion due to buoyant plume rise
x,y,z	W-E, S-N, and vertical coordinates, respectively
x_0, y_0	surface coordinates of source
$\tilde{z}$	dimensionless distance from adaptive volume center point
z_0	height of adaptive volume center point

Greek Letters

α	coefficient in power function representation of σ_y
γ	exponent in power function representation of σ_z
$\Delta(\,)$	increment
λ	coefficient in power function representation of σ_y
σ_V	velocity standard deviations
σ	material distribution standard deviation
η	dummy height variable in definition of $\tilde{z}$
ζ_m	horizontal displacements in sheared puff model of Shieh
ϕ	latitude
Ω	rotation rate of earth

Subscripts

$(\,)_g$	geostrophic value
$(\,)_h$	horizonal component
$(\,)_i$	adaptive volume vertical level index

$()_j$	Pasquill-Gifford stability class index
$()_m$	index in sheared puff model of Shieh
$()_{x,y,z}$	x, y , or z direction, respectively

Superscripts

$()'$	non-random turbulent fluctuation
$()''$	random turbulent fluctuation
$\overline{()}$	average value

LIST OF FIGURES

12. Modeled (squares) and analytical Gaussian (triangles) surface Lagrangian concentrations (10^{-4} g m^{-3}) under center of moving middle puff segment (of Fig. 11) for the uniform steady-state winds of Case a. Also shown is "best" computer graphic fit (solid line) to AVP results.

13. Modeled (squares) and analytical Gaussian (pluses) Eulerian concentrations (10^{-4} g m^{-3}) at fixed site (1.55 km east of source) at the surface for the uniform steady-state winds of Case a. Also shown is "best" computer graphic fit (solid line) to AVP results.

14. Modeled (squares) and analytical Gaussian (pluses) Eulerian concentrations (10^{-4} g m^{-3}) at fixed site (1.55 km east of source) at height of H/2 for the uniform steady-state winds of Case a. Also shown is "best" computer graphic fit (solid line) to AVP results.

15. Modeled (squares) and analytical Gaussian (pluses) Eulerian concentrations (10^{-4} g m^{-3}) at fixed site (1.55 km east of source) at the effective stack height for the uniform steady-state winds of Case a. Also shown is "best" computer graphic fit (solid line) to modeled results.

16. Eulerian concentrations histories (10^{-4} g m^{-3}) at four fixed sites (1.55, 2.5, 4.7 and 6.1 km east of source) at the effective stack height H, at H/2, and at surface for the uniform steady-state winds of Case a.

17. Ekman spiral lateral $\bar{u}$ (squares) and longitudinal $\bar{v}$ (triangles) wind components versus height.

18. Advection of model points (dots) and diffusive growth (horizontal line σ_h shown to scale) of single adaptive volume after 40 min travel with the positive wind speed shear of Case b. Dashed line corresponds to linear with height advection, and source shown by rectangle.

19. Lagrangian concentrations (10^{-4} g m^{-3}) at effective stack height H (every 10 min, starting at 60 min travel) at the grid point closest to center of moving middle puff segment for the uniform steady-state winds of Case a (squares), the positive wind speed shear of Case b (triangles), the positive directional shear of Case c (diamonds), and fumigation conditions of Case e (pulses). Because of the subsidence velocity of Case d (exes), concentration values at H are not at puff center.

20. Longitudinal axial concentration (10^{-4} g m^{-3}) cross section after 30 min travel with the positive wind speed shear of Case b.

21. Longitudinal axial concentration (10^{-4} g m^{-3}) cross section after 60 min travel with the positive wind speed shear of Case b.

22. Advection of center point (dots) and lateral diffusive growth (horizontal line σ_h shown to scale) of puff during first 160 min travel with the directional shear of Case c. Also shown is trajectory of a puff (dashed-line) with uniform steady-state westerly wind and source location (rectangle).

23. Lateral concentration (10^{-4} g m^{-3}) cross section after 40 min travel (1.1 km east of source) with the positive wind directional shear of Case c.

24. Lateral concentration (10^{-4} g m^{-3}) cross section after 60 min travel (1.6 km east of source) with the positive wind directional shear of Case c.

25. Surface Lagrangian concentrations (10^{-4} g m^{-3}) under center of moving middle puff segment (every 10 min, starting at 40 min of travel) for the uniform steady-state winds of Case a (squares), the positive directional shear of Case c (triangles), the subsidence velocity of Case d (diamonds) and the fumigation conditions of Case e (exes).

26. Subsidence velocity profile used for Case d, with source height shown as square.

27. Advection of center point (dots) and lateral diffusive growth (horizontal line σ_h shown to scale) of puff during first 160 min travel with the subsidence velocity of Case d. Source location shown by rectangle.

28. Longitudinal axial concentration (10^{-4} g m^{-3}) cross section after 60 min travel with the subsidence velocity of Case d.

29. Temporal variation of depth of layer h_c in which Pasquill-Gifford class A stability replaces class B stability.

30. Advection of model points (dots) and diffusive growth (horizontal line σ_h shown to scale) of single adaptive volume after 30 min travel with the fumigation conditions of Case e. Source location shown by rectangle.

31. Longitudinal axial concentration (10^{-4} g m^{-3}) cross section after 60 min travel with the fumigation conditions of Case e.

32. Longitudinal axial concentration (10^{-4} g m^{-3}) cross section after 110 min travel with the fumigation conditions of Case e.

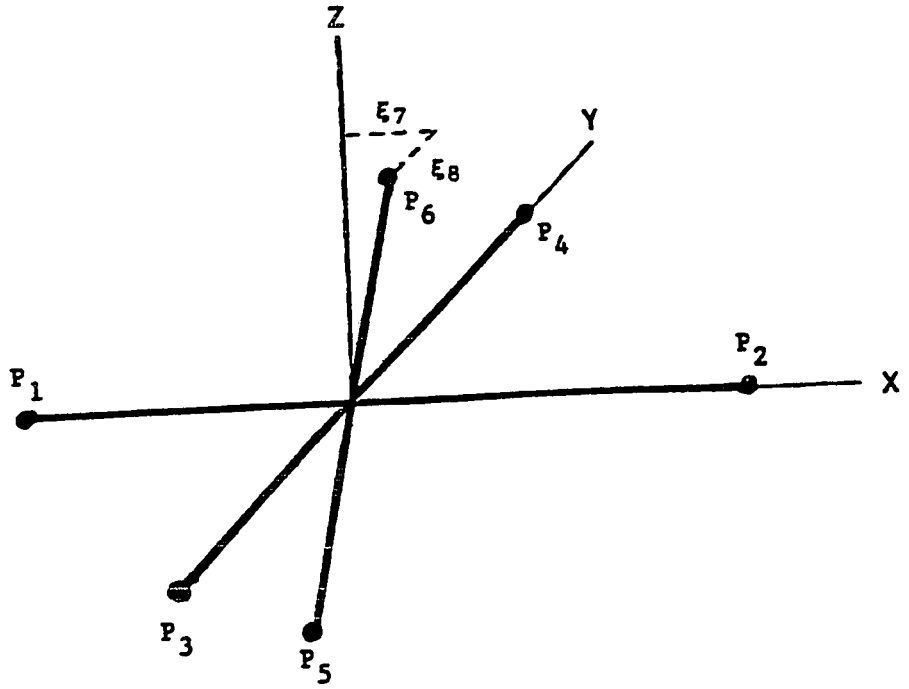

Fig.1

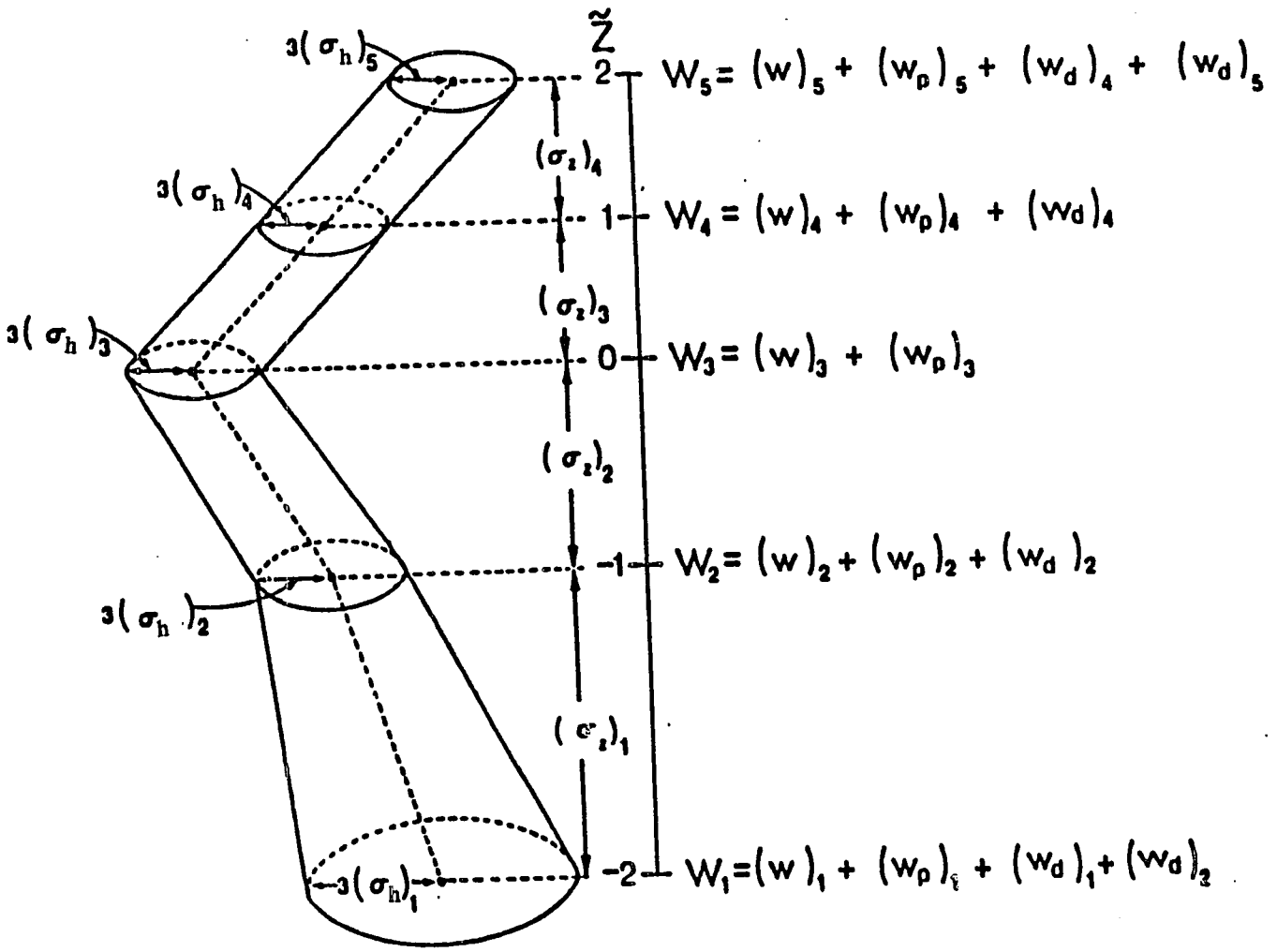
$\tilde{Z}$
$3(\sigma_h)_5$
$3(\sigma_h)_4$
$3(\sigma_h)_3$
$3(\sigma_h)_2$
$3(\sigma_h)_1$
$(\sigma_z)_4$
$(\sigma_z)_3$
$(\sigma_z)_2$
$(\sigma_z)_1$
2
1
0
-1
-2
$W_5 = (w)_5 + (w_p)_5 + (w_d)_4 + (w_d)_5$
$W_4 = (w)_4 + (w_p)_4 + (w_d)_4$
$W_3 = (w)_3 + (w_p)_3$
$W_2 = (w)_2 + (w_p)_2 + (w_d)_2$
$W_1 = (w)_1 + (w_p)_1 + (w_d)_1 + (w_d)_2$

Fig.2

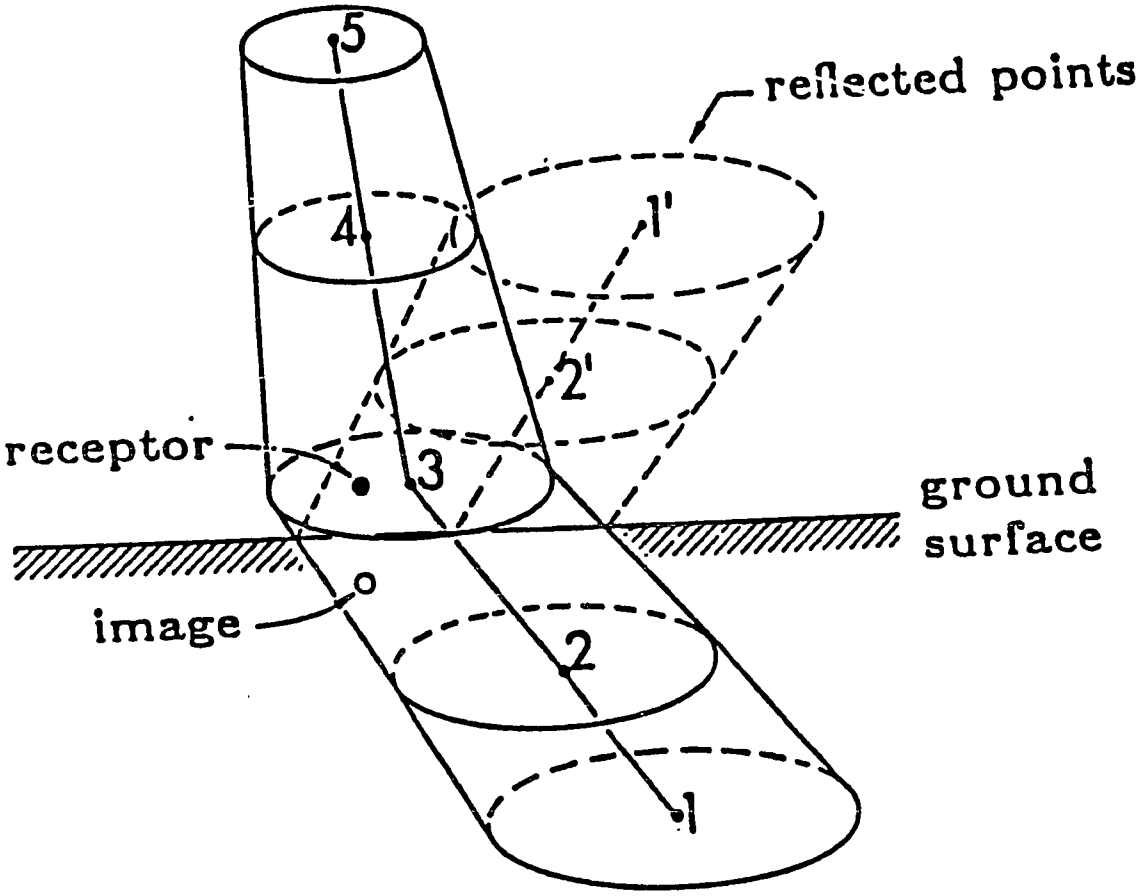

Fig.3

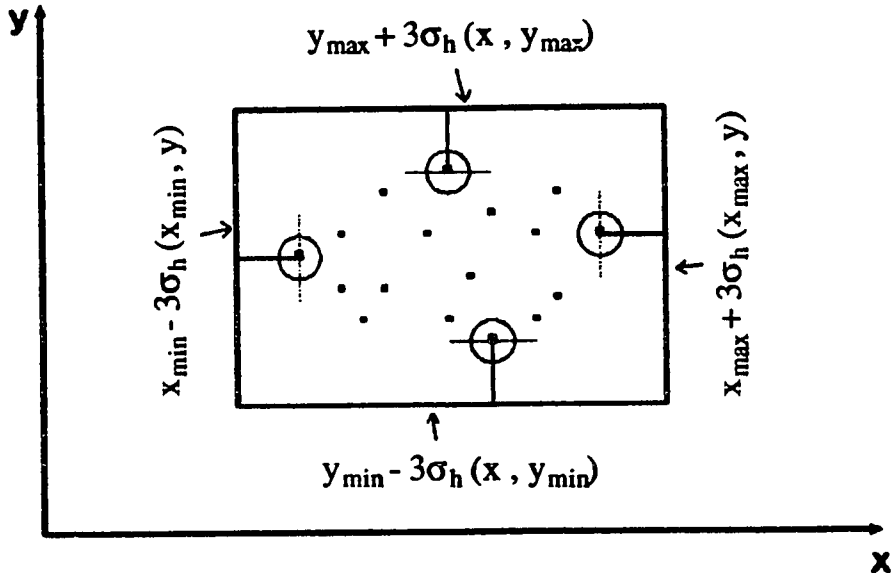
y
x
$y_{max} + 3\sigma_h (x , y_{max})$
$x_{min} - 3\sigma_h (x_{min} , y)$
$x_{max} + 3\sigma_h (x_{max} , y)$
$y_{min} - 3\sigma_h (x , y_{min})$

Fig.4

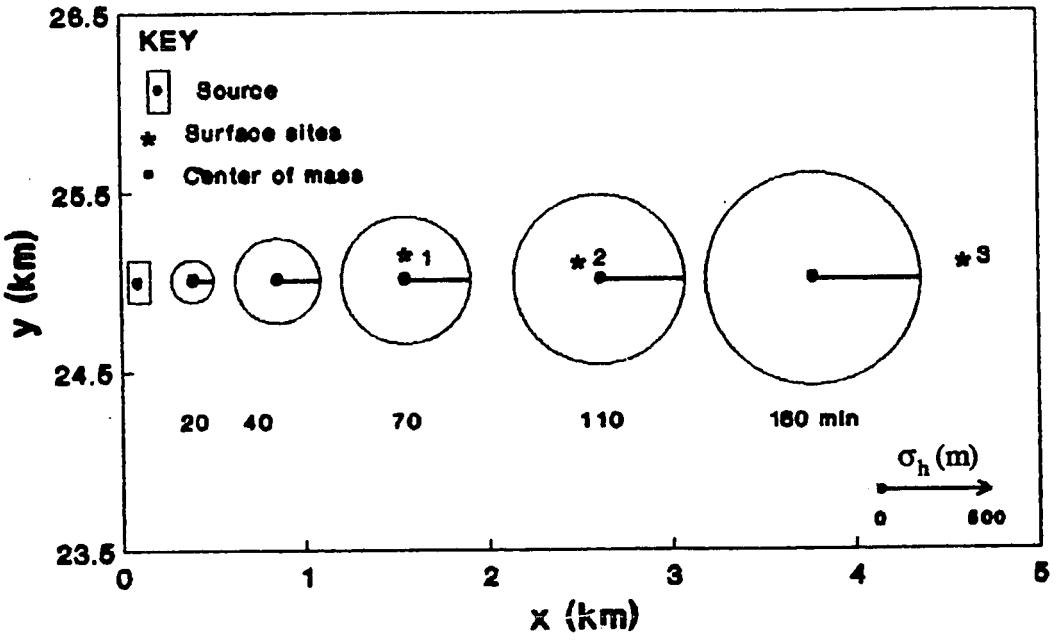
KEY
Source
Surface sites
Center of mass
26.5
25.5
24.5
23.5
y (km)
0
1
2
3
4
5
x (km)
1
2
3
20
40
70
110
160 min
σh (m)
0
600

Fig.5

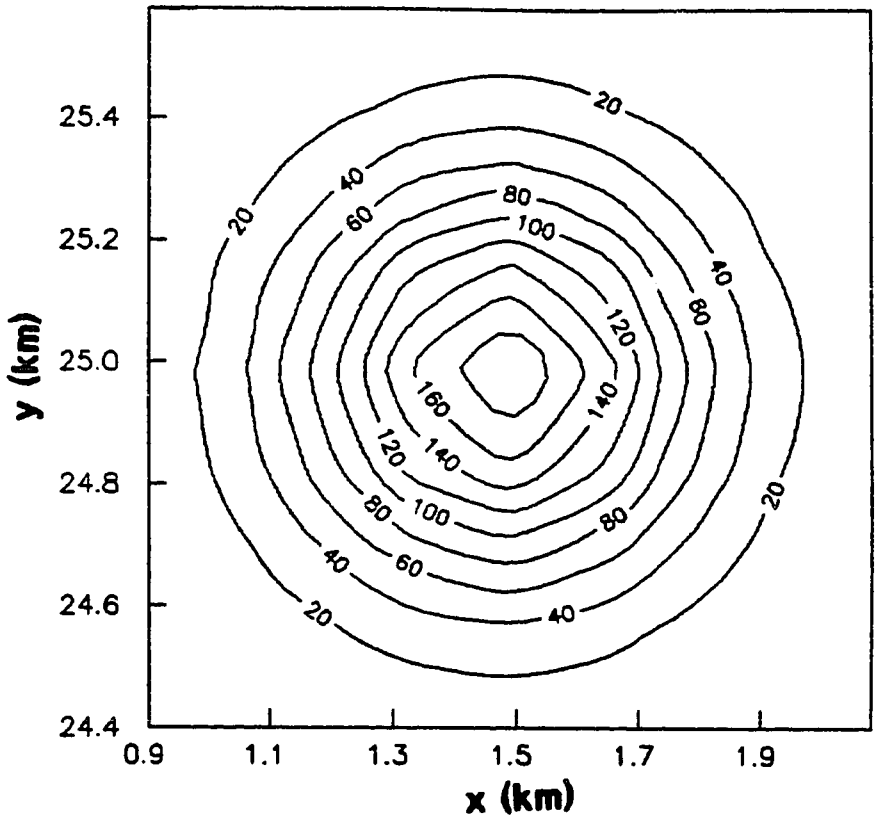
25.4
25.2
25.0
24.8
24.6
24.4
y (km)
0.9
1.1
1.3
1.5
1.7
1.9
x (km)
20
40
60
80
100
120
140
160

Fig.6

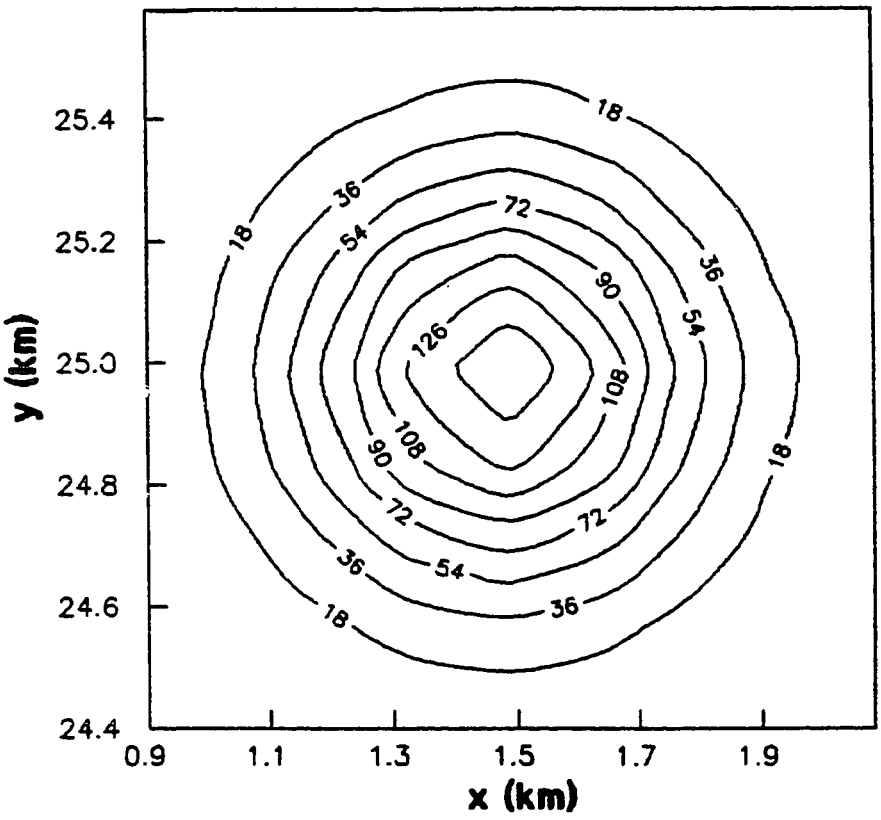
25.4
25.2
25.0
24.8
24.6
24.4
y (km)
0.9
1.1
1.3
1.5
1.7
1.9
x (km)
18
36
54
72
90
108
126

Fig.7

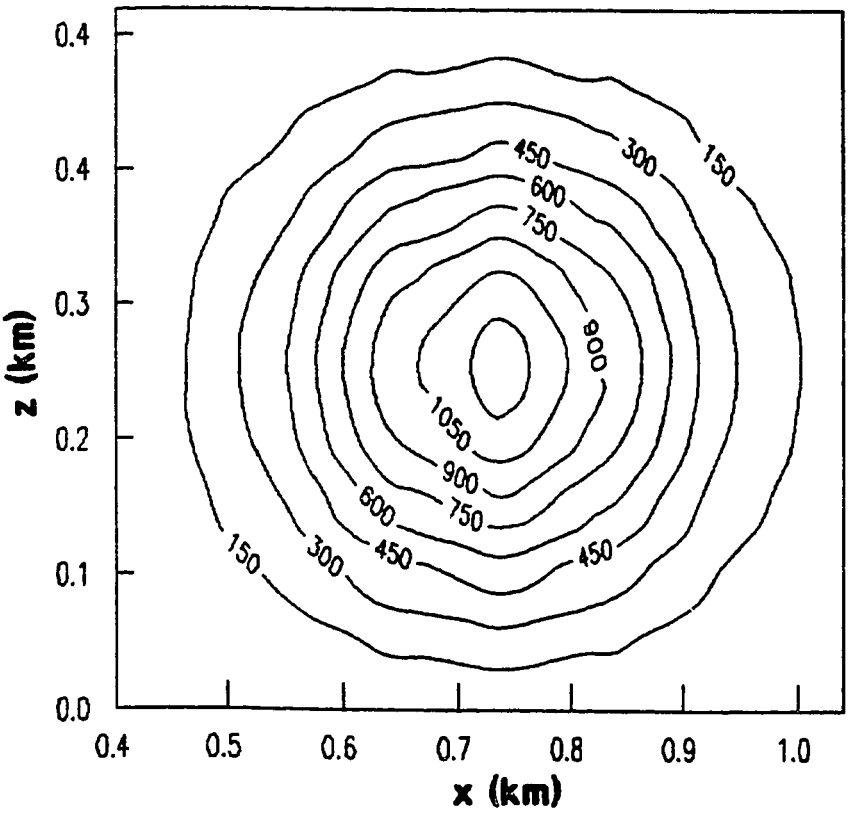
0.4
0.4
0.3
0.2
0.1
0.0
z (km)
0.4
0.5
0.6
0.7
0.8
0.9
1.0
x (km)
150
300
450
600
750
900
1050
900
750
600
450
300
150
450
600
750
900
450

Fig.8

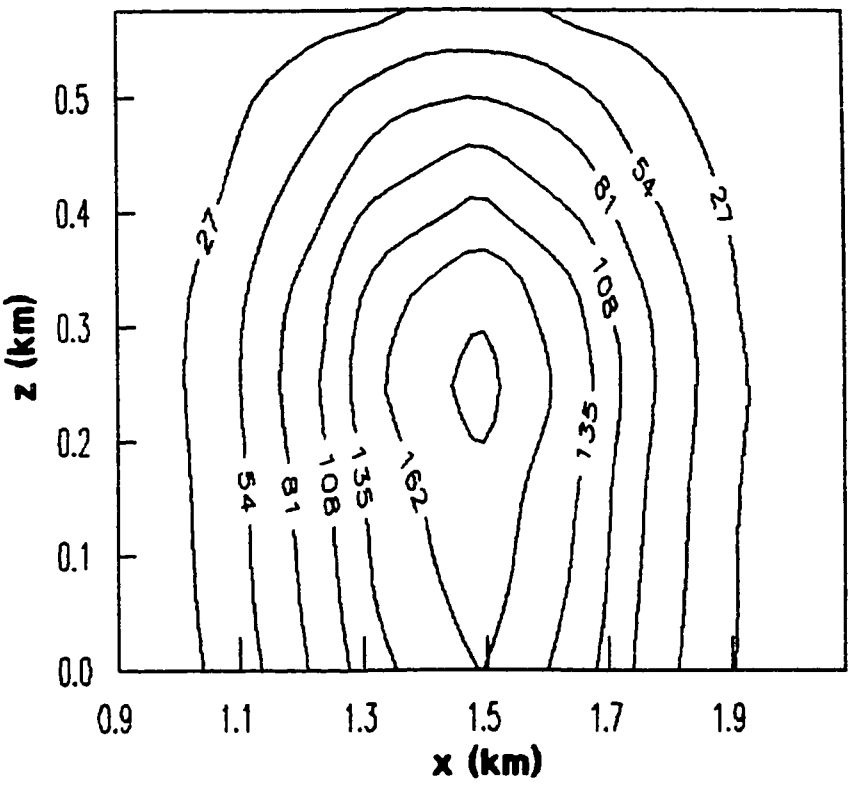
0.5
0.4
0.3
0.2
0.1
0.0
z (km)
0.9
1.1
1.3
1.5
1.7
1.9
x (km)
27
54
81
108
135
162
135
108
81
54
27

Fig.9

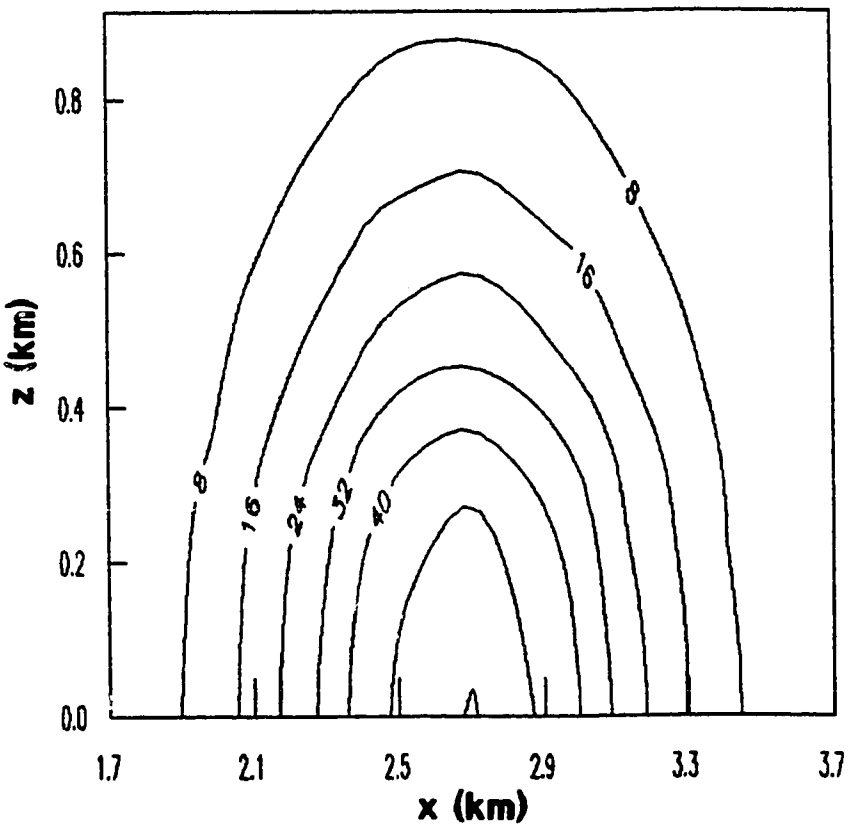

Fig.10

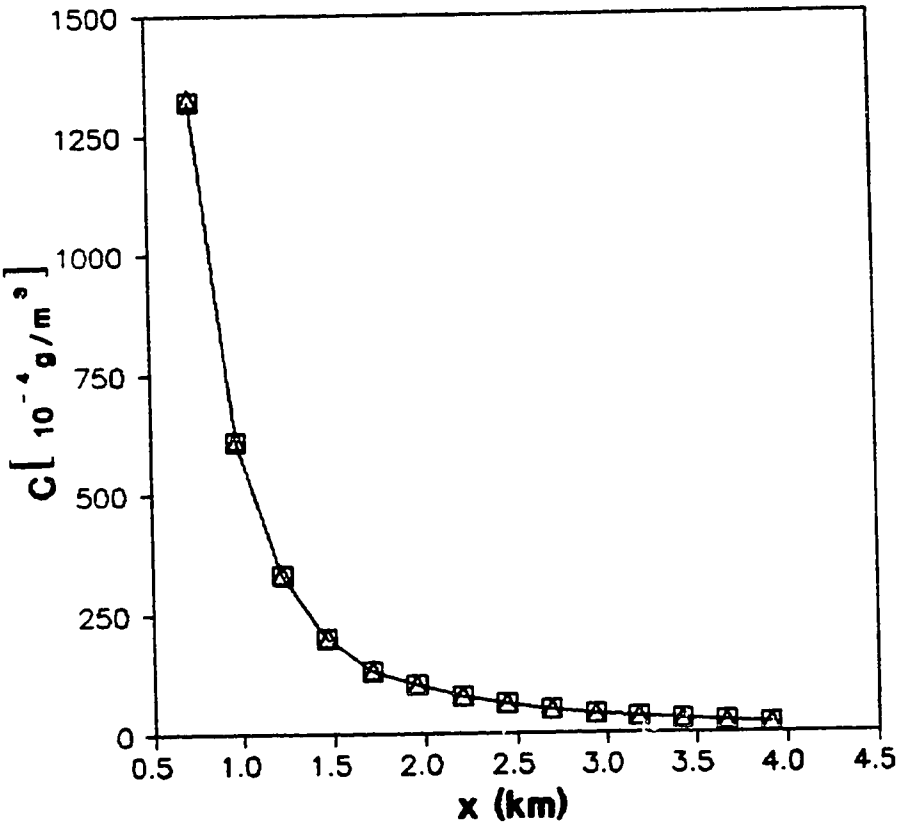
1500
1250
1000
750
500
250
0
C[10⁻⁴ g/m³]
0.5
1.0
1.5
2.0
2.5
3.0
3.5
4.0
4.5
x (km)

Fig.11

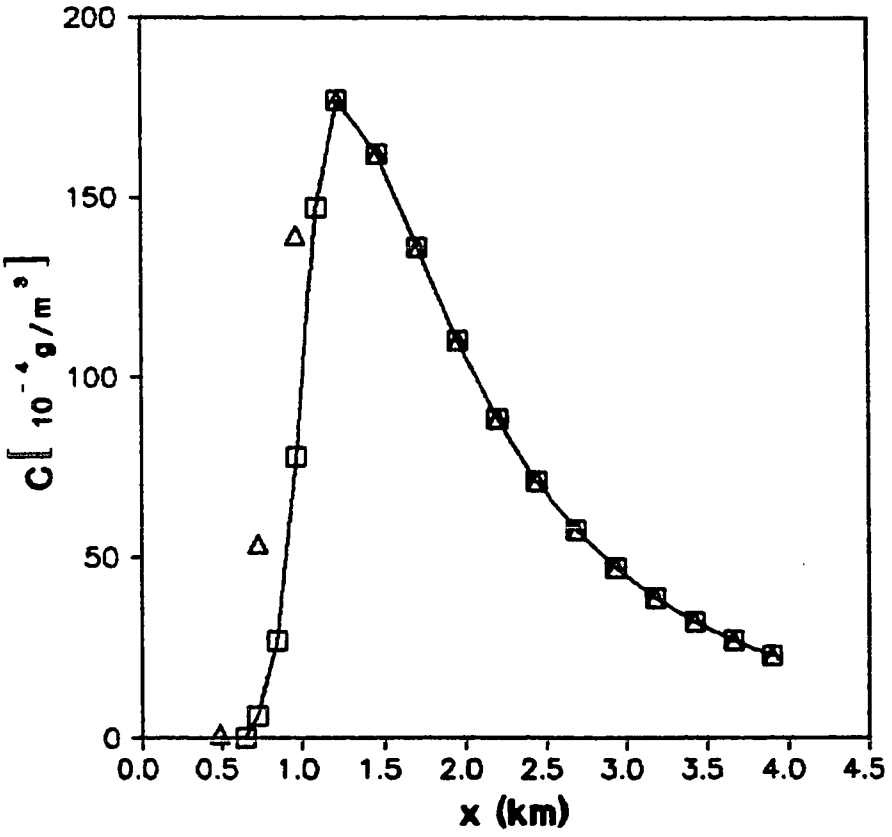

Fig.12

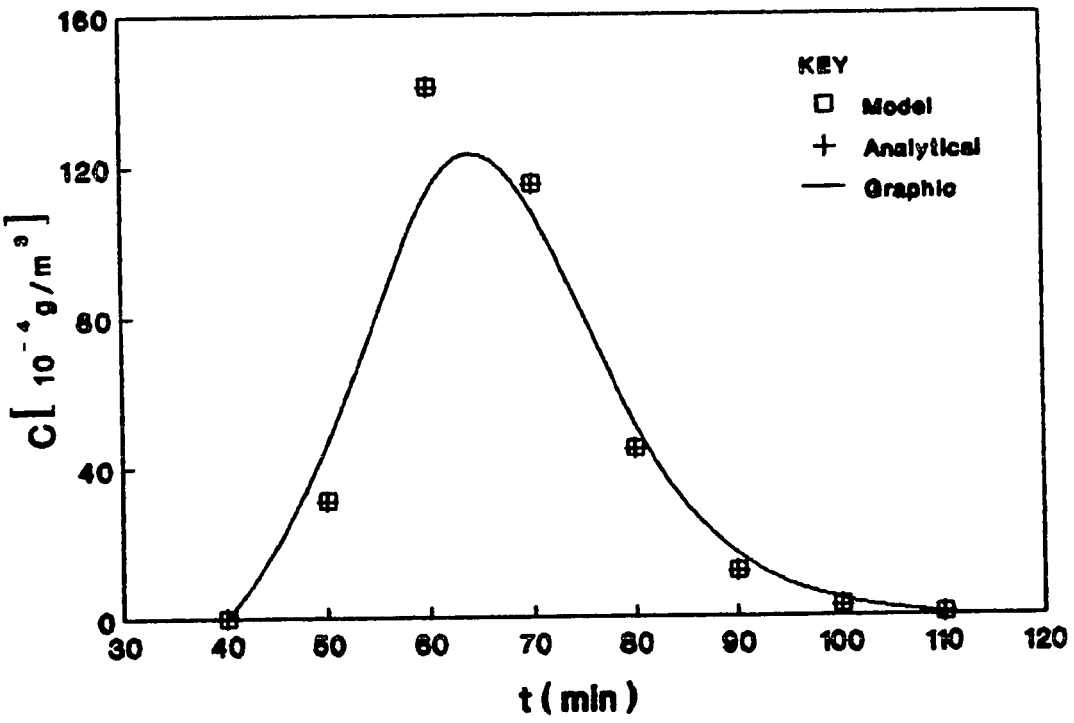
160
120
80
40
0
C[10⁻⁴ g/m³]
30
40
50
60
70
80
90
100
110
120
t (min)
KEY
Model
Analytical
Graphic

Fig.13

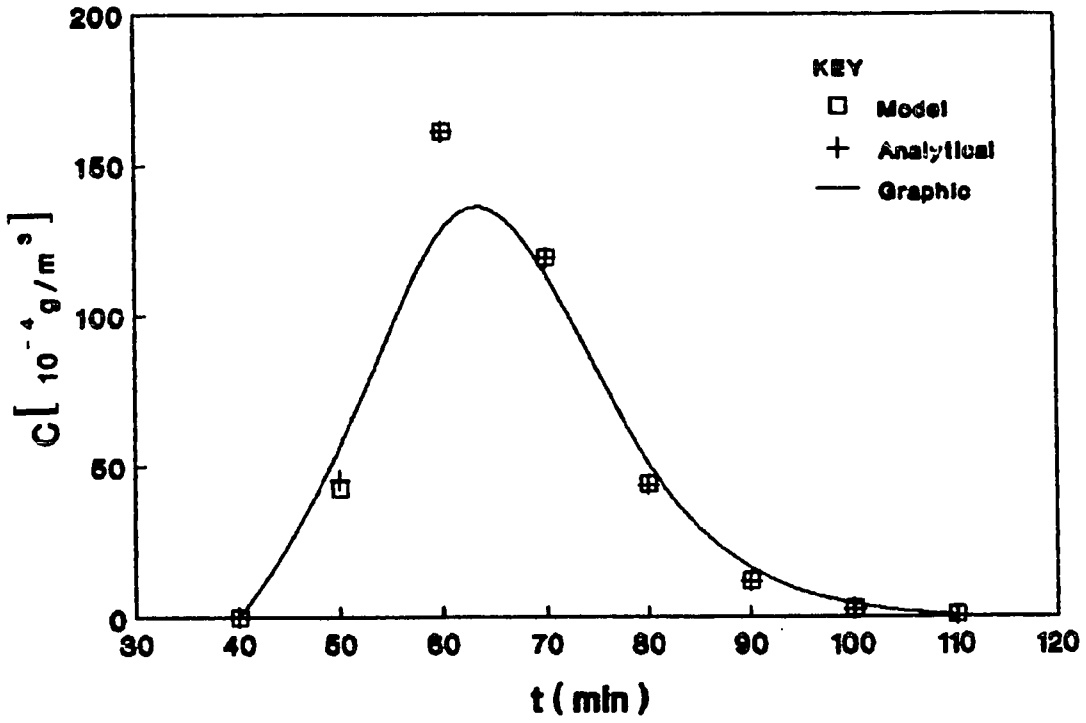
200
150
100
50
0
C[10⁻⁴ g/m³]
30
40
50
60
70
80
90
100
110
120
t (min)
KEY
Model
Analytical
Graphic

Fig.14

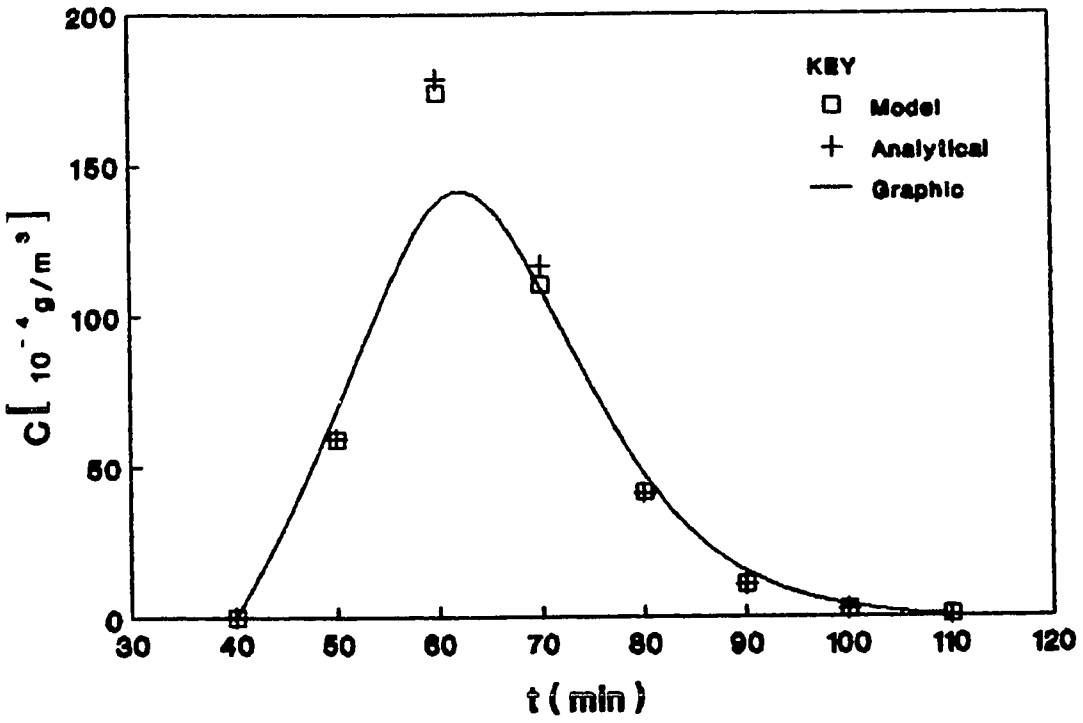
200
150
100
50
0
C[10⁻⁴ g/m³]
30
40
50
60
70
80
90
100
110
120
t (min)
KEY
Model
Analytical
Graphic

Fig.15

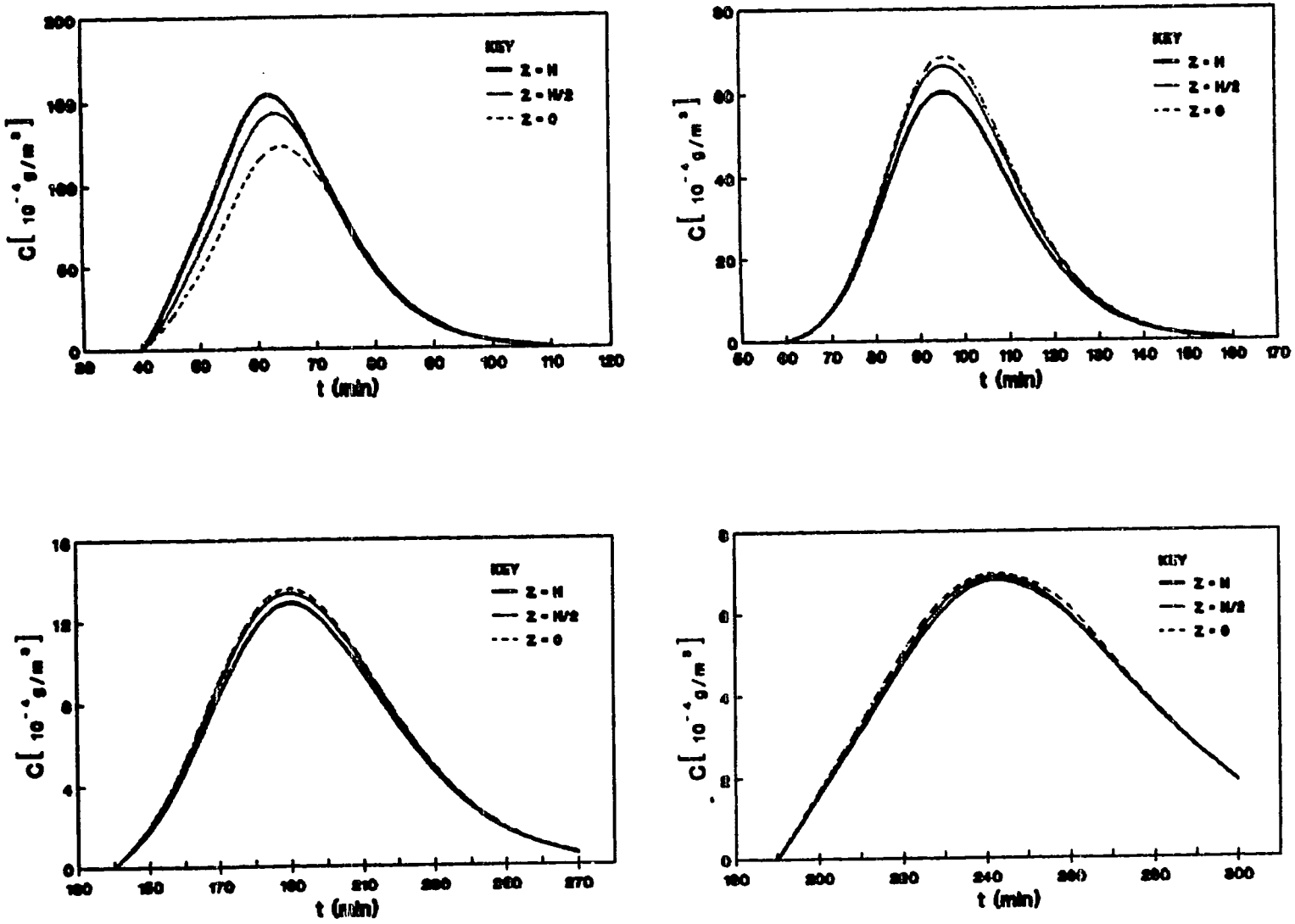

Fig.16

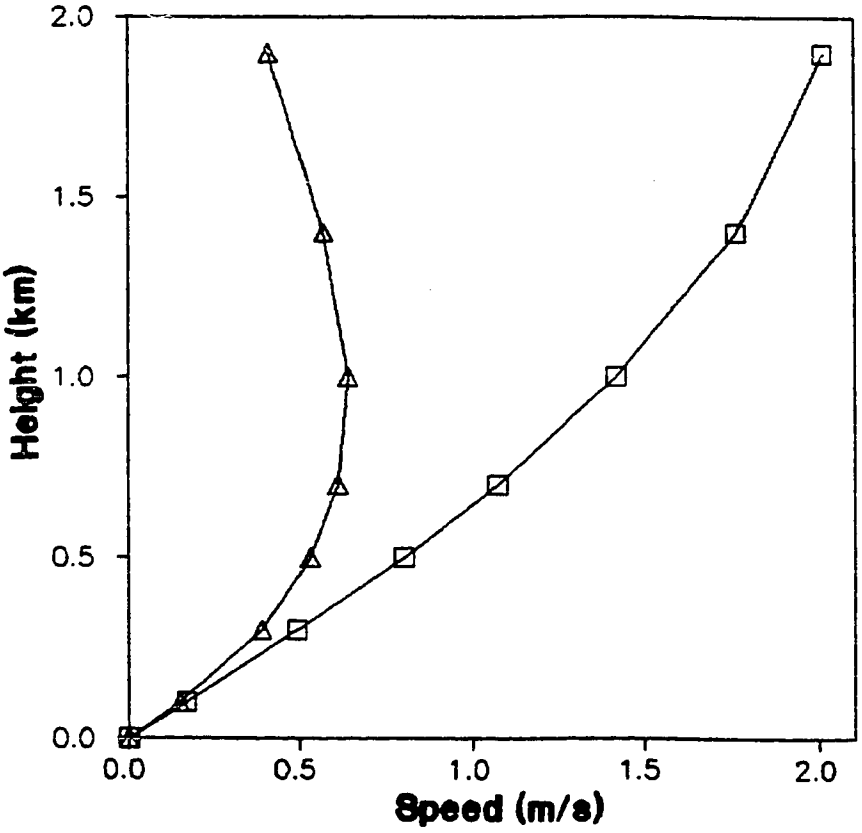

Fig.17

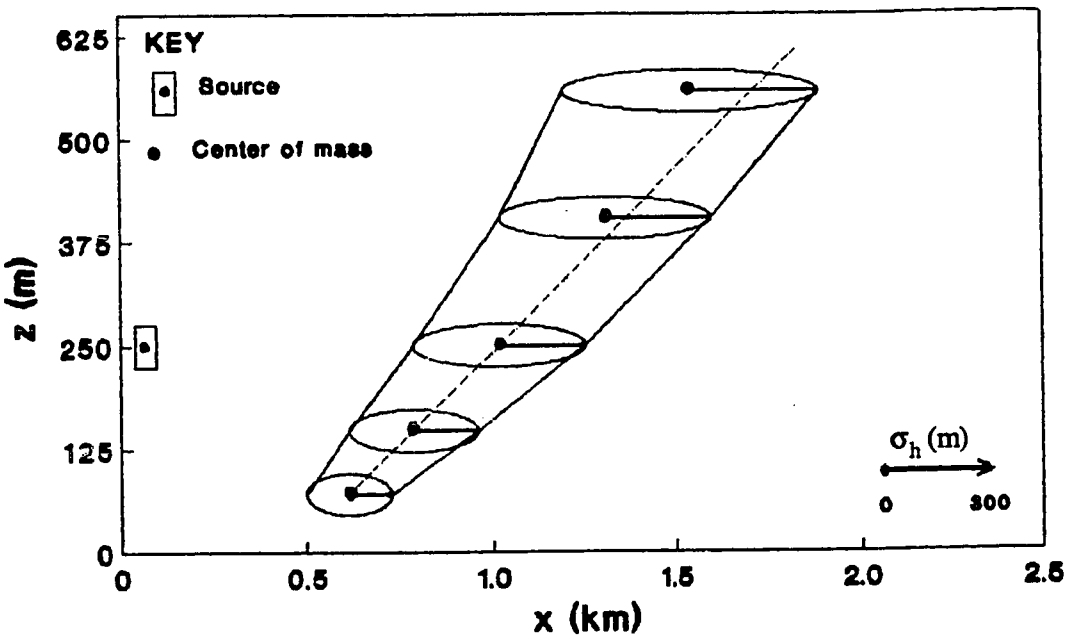
KEY
Source
Center of mass
625
500
375
250
125
0
z (m)
0
0.5
1.0
1.5
2.0
2.5
x (km)
σ_h (m)
0
300

Fig.18

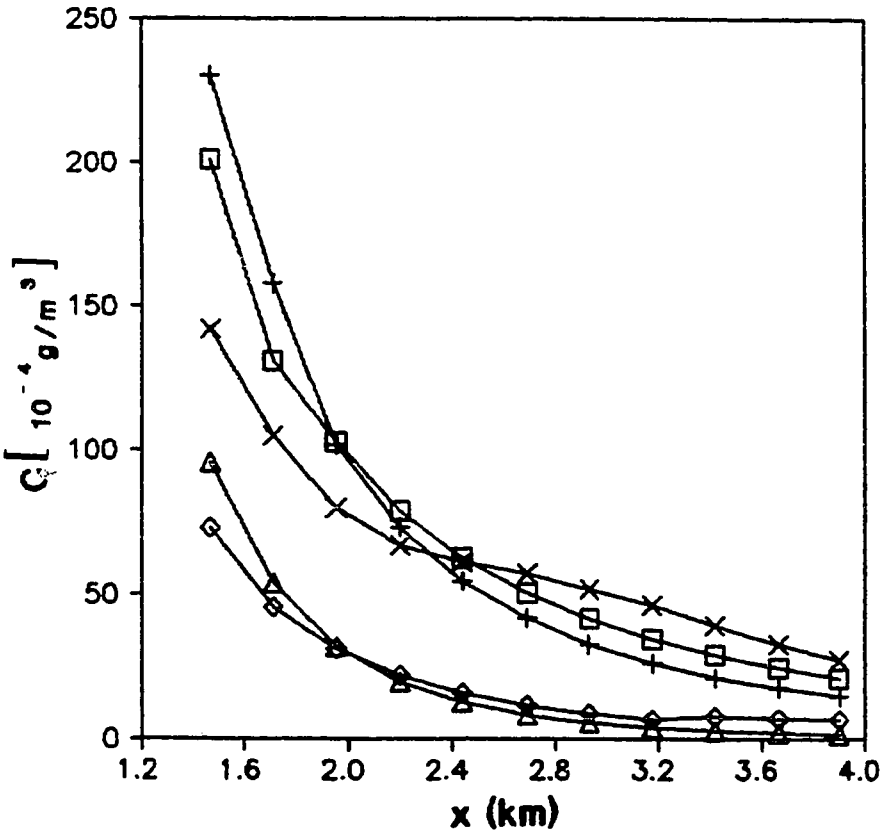

Fig.19

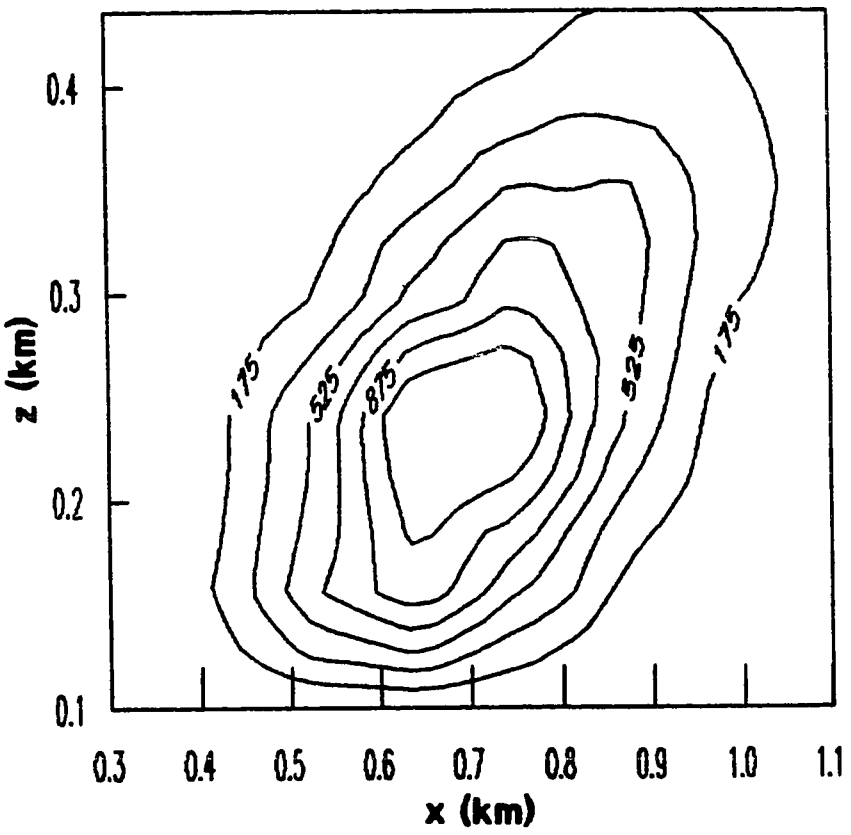

Fig.20

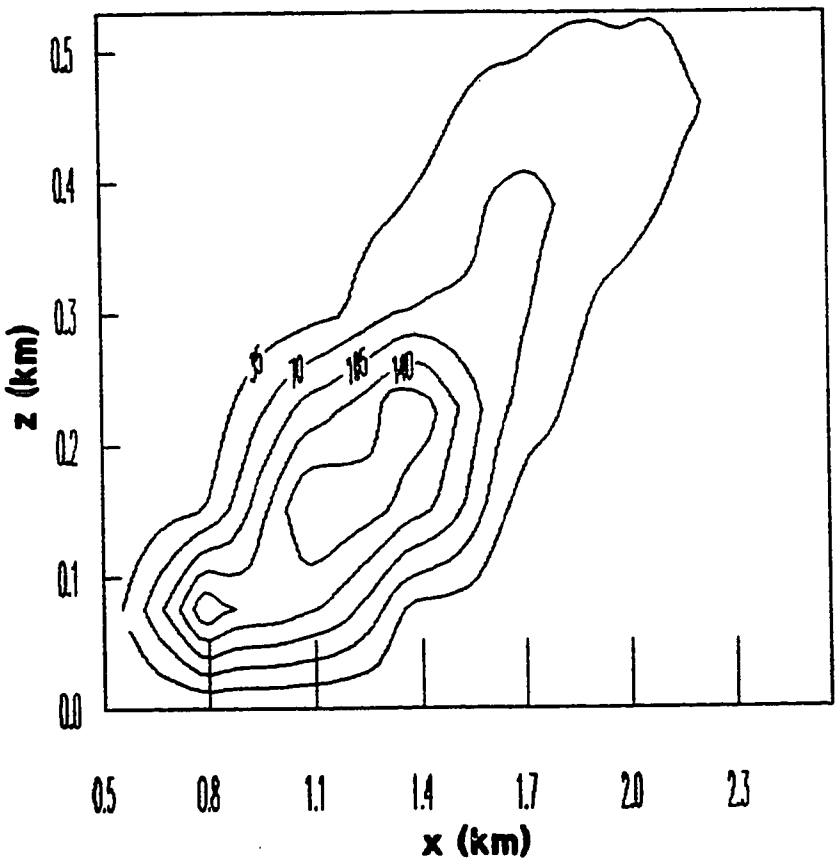

Fig.21

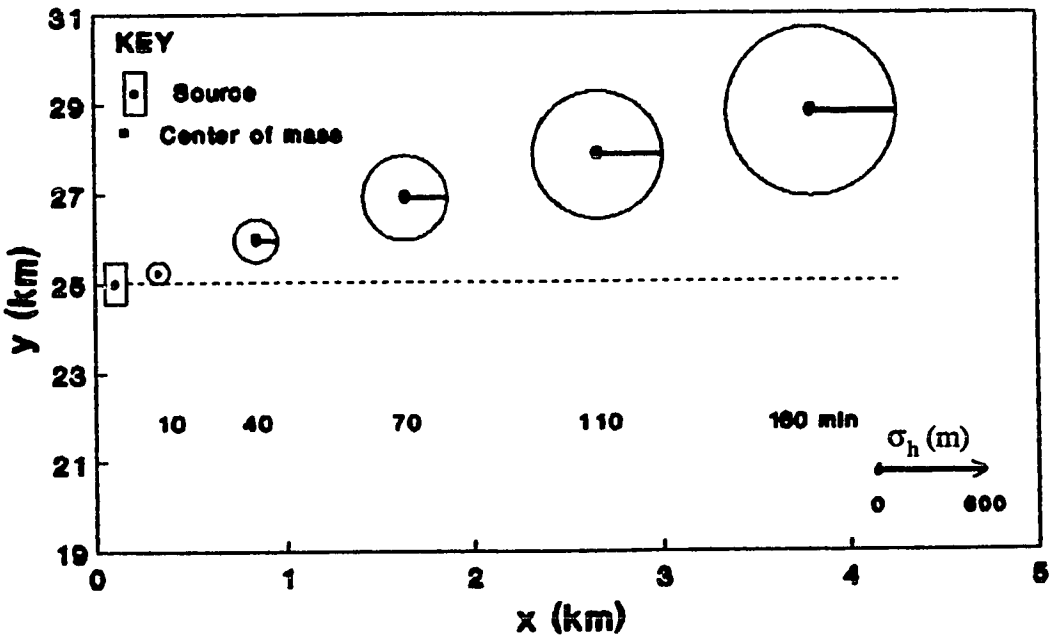
KEY
Source
Center of mass
10
40
70
110
160 min
σ_h (m)
0
600
y (km)
x (km)
31
29
27
25
23
21
19
0
1
2
3
4
5

Fig.22

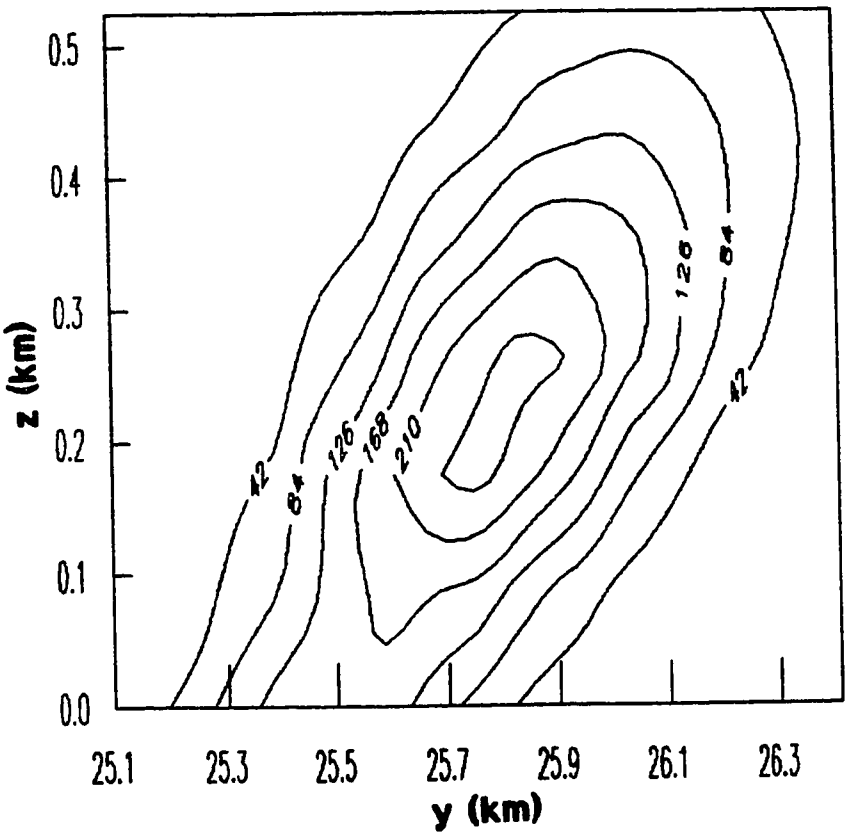
0.5
0.4
0.3
0.2
0.1
0.0
z (km)
25.1
25.3
25.5
25.7
25.9
26.1
26.3
y (km)
42
64
126
168
210
126
64
42

Fig.23

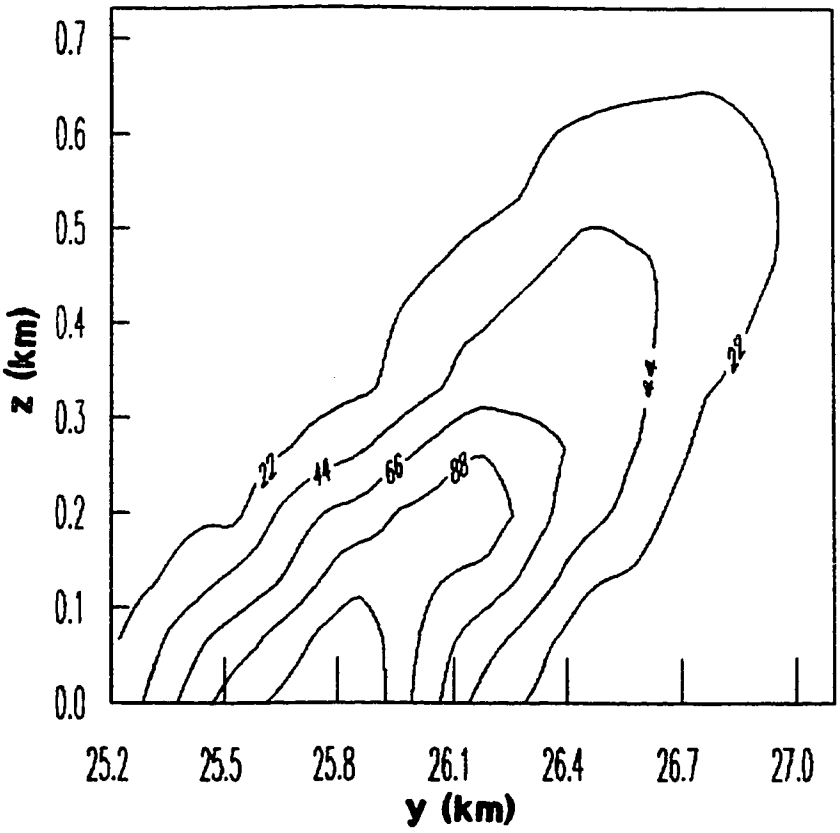
0.7
0.6
0.5
0.4
0.3
0.2
0.1
0.0
z (km)
22
44
66
88
44
22
25.2
25.5
25.8
26.1
26.4
26.7
27.0
y (km)

Fig.24

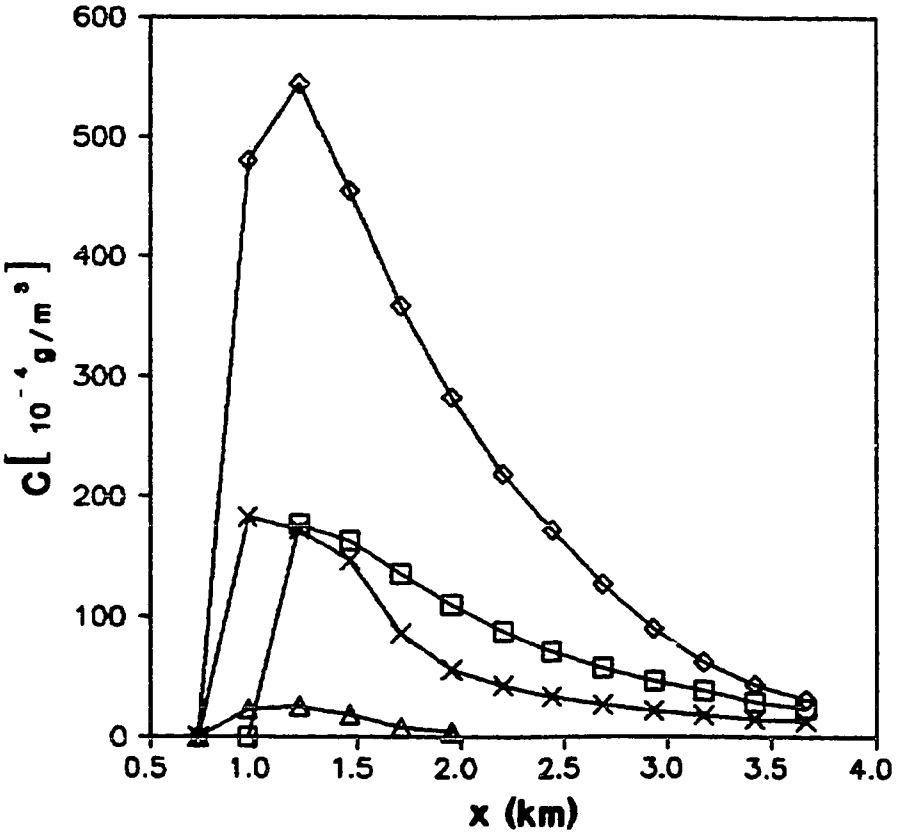

Fig.25

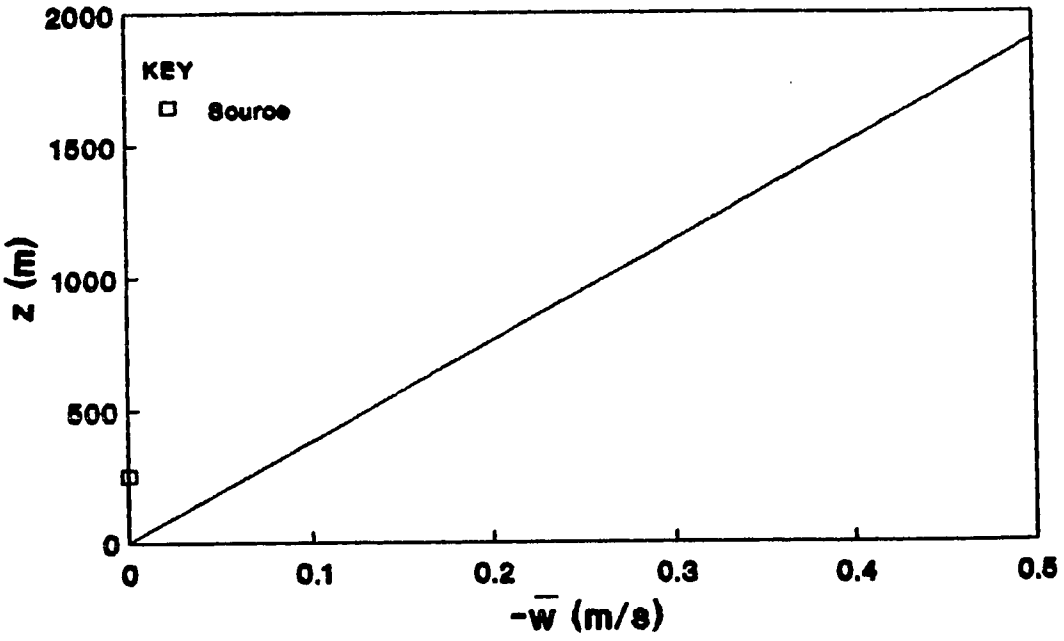

Fig.26

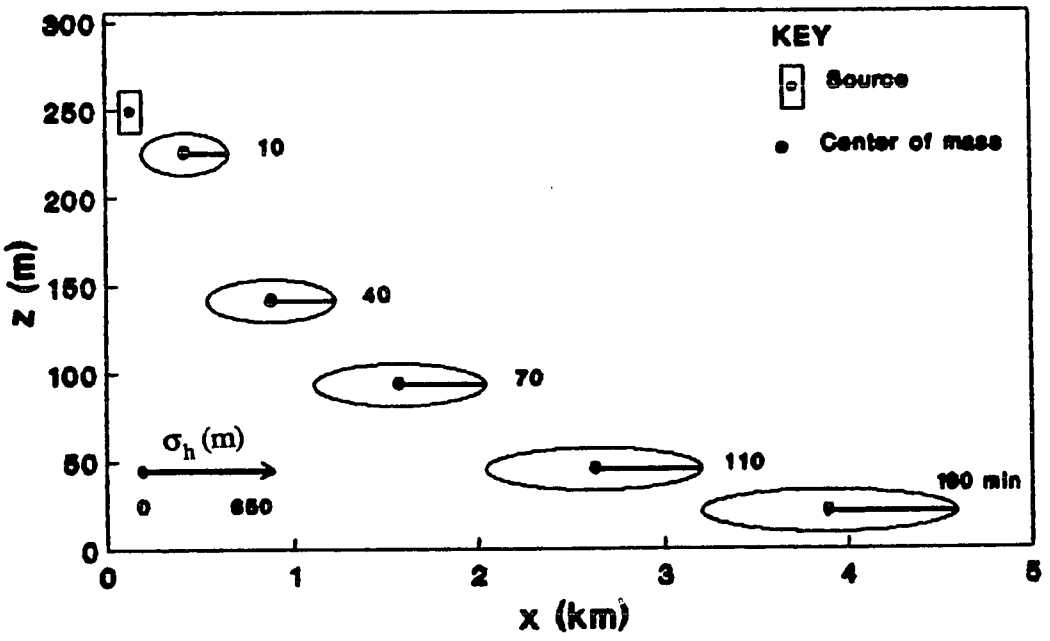
KEY
Source
Center of mass
10
40
70
110
190 min
σ_h (m)
0
650
300
250
200
150
100
50
0
N (E)
0
1
2
3
4
5
x (km)

Fig.27

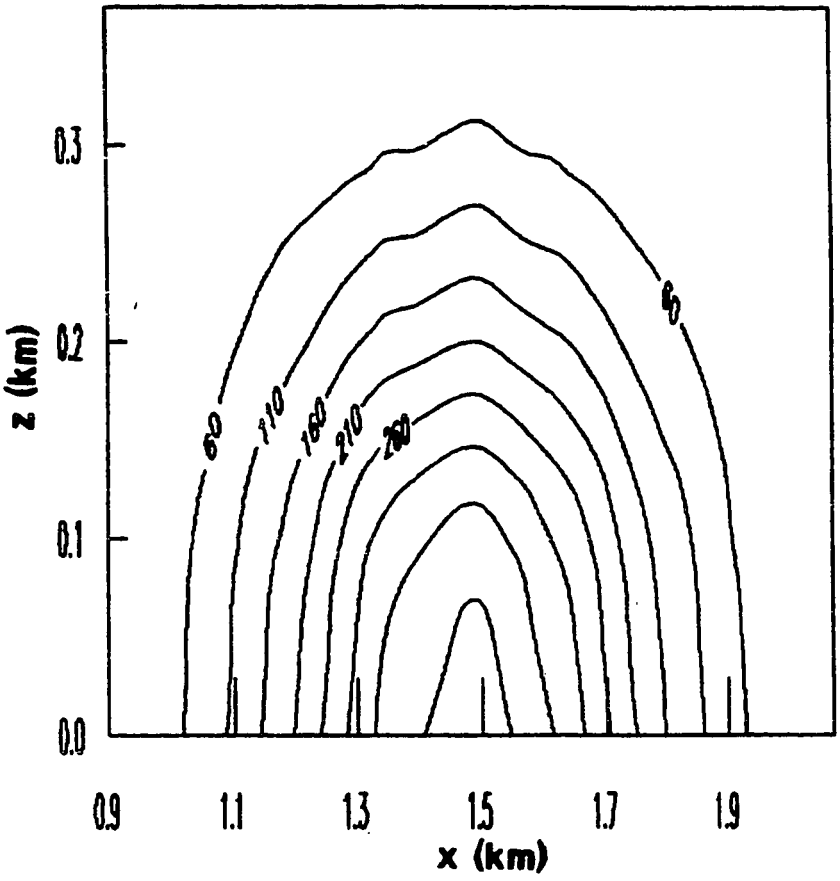

Fig.28

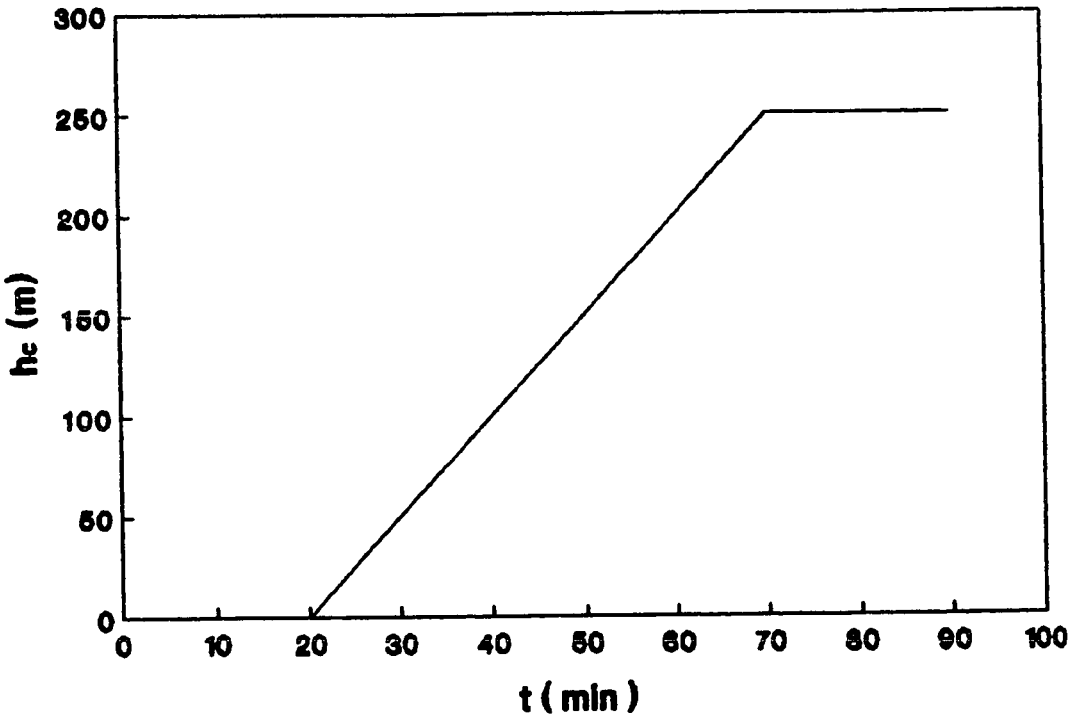

Fig.29

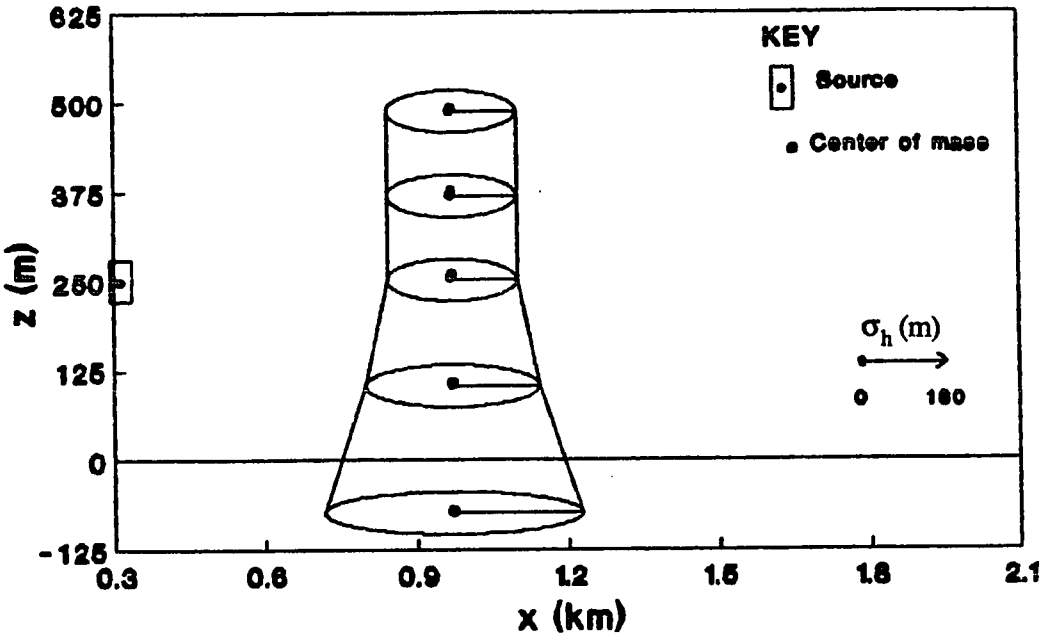
625
500
375
250
125
0
-125
z (m)
0.3
0.6
0.9
1.2
1.5
1.8
2.1
x (km)
KEY
Source
Center of mass
σ_h (m)
0
160

Fig.30

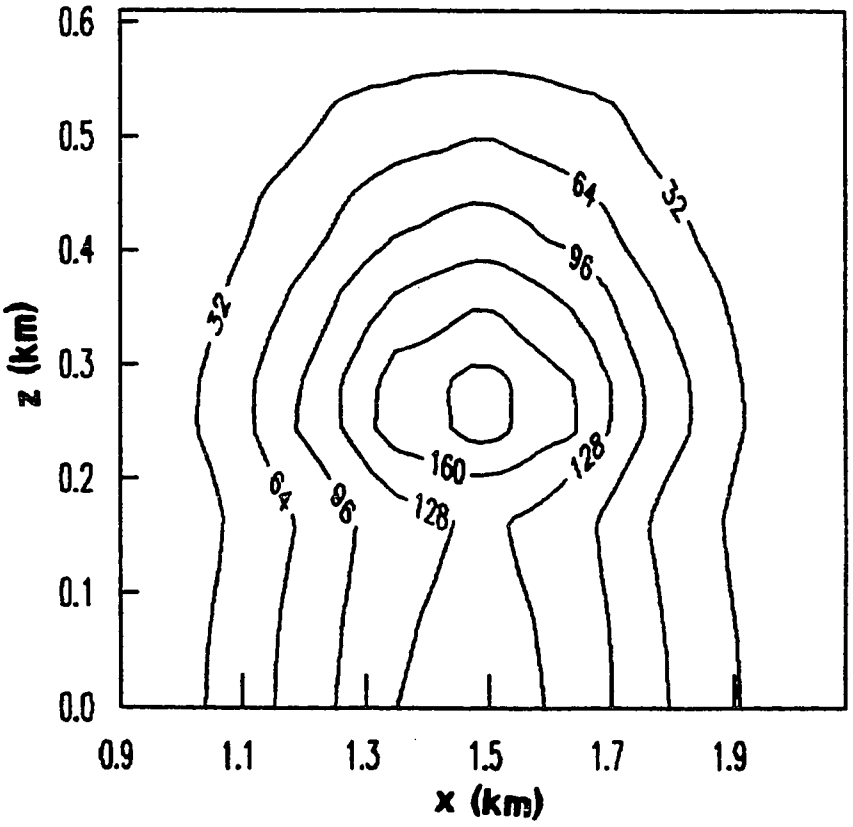
0.6
0.5
0.4
0.3
0.2
0.1
0.0
z (km)
0.9
1.1
1.3
1.5
1.7
1.9
x (km)
32
64
96
128
160
32
64
96
128

Fig.31

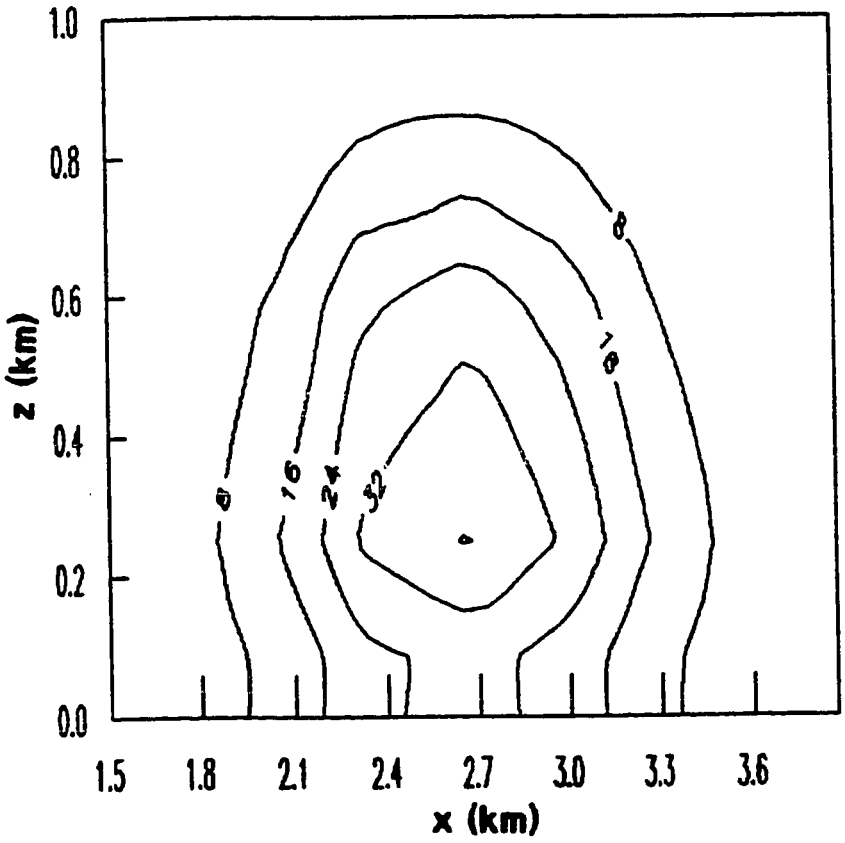

Fig.32